A ubiquitous spectrolaminar motif of local field potential power across the primate cortex

Diego Mendoza-Halliday* [a], Alex J. Major* [b], Noah Lee [a], Maxwell Lichtenfeld [c], Brock Carlson [c,d,e], Blake Mitchell [c,d,e], Patrick D. Meng [c], Yihan (Sophy) Xiong [c], Jacob Westerberg [c,d,e], Alexander Maier [c,d,e], Robert Desimone** [c,d,e], Earl K. Miller** [b], André M. Bastos** [c,d,e,f]

* equally-contributing first authors
** equally-contributing senior authors
a. McGovern Institute for Brain Research, Massachusetts Institute of Technology, Cambridge, MA, USA
b. The Picower Institute for Learning and Memory, Massachusetts Institute of Technology, Cambridge, MA, USA
c. Department of Psychology, Vanderbilt University, Nashville, TN, USA
d. Vanderbilt Vision Research Center, Vanderbilt University, Nashville, TN, USA
e. Vanderbilt Brain Institute, Vanderbilt University, Nashville, TN, USA
f. Corresponding author

Abstract

The mammalian cerebral cortex is anatomically organized into a six-layer motif. It is currently unknown whether a corresponding laminar motif of neuronal activity exists across the cortex. Here, we report the discovery of such a motif in the power of local field potentials (LFP). We implanted multicontact laminar probes in five macaque monkeys and recorded activity across layers in 12 cortical areas at various hierarchical processing stages in all cortical lobes. The anatomical laminar locations of recordings were histologically identified via electrolytic lesions. In all areas, we found a common spectrolaminar pattern characterized by an increasing deep-to-superficial layer gradient of gamma frequency LFP power peaking in layers 2/3, and an increasing superficial-to-deep gradient of alpha-beta power peaking in layers 5/6. Our results show a functional dissociation between superficial and deep layers that is preserved across the cortex, suggesting a ubiquitous layer and frequency-based mechanism for cortical computation.

Introduction

One of the most prominent structures of the mammalian brain is the cerebral cortex, a large mantle that covers most other structures and is thought to underlie some of the most complex functions and behaviors. One striking observation is that despite the vast diversity of functions carried out by different areas of the cortex, almost all of these areas share a ubiquitous anatomical motif composed of six distinct layers, with relatively minor variations across cortical areas and mammalian species [1]. This has led to the hypothesis that all cortical areas are composed of a common canonical microcircuit that is the fundamental unit for cortical computation [2–4]. This hypothesis implies that by understanding the fundamental computational principles of the canonical microcircuit, one should be able to explain how all areas of the cortex accomplish their respective functions with precise variations of the ubiquitous anatomical motif. This influential hypothesis has inspired many theoretical proposals for cortical function [5–7].

It is reasonable to predict that the marked anatomical differences between cortical layers in cell size, composition, and projection patterns give rise to marked differences in the patterns of neuronal activity between these layers. Characterizing and investigating these ubiquitous functional differences will be one of the most fundamental steps towards understanding the mechanisms underlying the canonical microcircuit and its computational principles. Importantly, because the overall six-layer anatomical motif is relatively preserved across cortical areas and across individual subjects, the laminar activity differences should also be preserved across cortical areas [8,9] and subjects in order to qualify as a functional correlate of the anatomical motif. Moreover, in all cortical areas and subjects, the activity differences should consistently map onto the same anatomical landmarks with respect to the laminar architecture.

While differences in neuronal activity between cortical layers have been observed by numerous studies [10–18], these differences have typically been observed in a given cortical area and in the context of a given function, not as a common phenomenon across the cortex. No study to our knowledge has examined laminar-resolved electrophysiological recordings across early, middle, and late stages of hierarchical processing and sought to identify common laminar features across areas. To date, the only pattern of activity that that has been proposed to reflect the ubiquitous laminar motif of the cortex consists of a canonical laminar activation: thalamocortical and/or feedforward inputs first excite layer 4, which in turn activates layers 2/3, which then activate layers 5/6 [4,19]. Using current source density (CSD) analysis of local field potentials[20], this activation pattern has been observed in visual cortex in the form of current sinks and sources. The pattern is currently used as a gold standard for estimating the relative location of cortical layers in anatomical recordings [21,22]. However, the generality of this circuitry has been questioned by the observation that deep layers can be activated independently of superficial layers [23].

It has also been proposed that cortex generates a canonical laminar pattern of oscillatory activity composed of gamma rhythms (50 – 100 Hz) in superficial layers and alpha-beta (10 – 30 Hz) rhythms in deep layers [5,10,12,16,24–28]. According to this proposal, these rhythms may traffic feedforward activity through superficial layer gamma and feedback activity through deep layer alpha-beta [25,29–32]. This proposal is supported by observations in early visual cortex and prefrontal cortex that the power of local field potential (LFP) oscillations is highest in superficial cortex at gamma frequencies and in deep cortex at alpha-beta frequencies [10,33]. Others have challenged the generality of these findings [13,34] by observing that local re-referencing switches results in higher alpha-beta power in superficial layers.

Whether the cortex contains canonical layer-specific oscillatory mechanisms, and whether these are preserved across all cortical areas, remains unknown. To investigate this, we recorded LFP signals across all cortical layers using multicontact laminar probes. We combined data collected in three different labs from five monkeys and twelve cortical areas ranging across a wide variety of hierarchical processing stages and functions (Fig. 1a): V1 (primary visual cortex), V4 and middle temporal or MT (early visual areas), medial superior temporal or MST (a visual association and multimodal area), medial intraparietal or MIP (a visual/somatosensory/somatomotor area), area 5 (somatosensory cortex), area 6 (premotor cortex), 7A and lateral intraparietal or LIP (higher-order parietal association areas), and right and left lateral prefrontal cortex or LPFC (a higher-order executive area).

We observed a laminar pattern of LFP relative power characterized by higher power in the gamma frequencies in superficial layers and higher power in the alpha-beta frequencies in deep layers. Furthermore, this spectrolaminar motif was ubiquitous in all cortical areas studied and was more preserved between areas than the pattern of CSD sinks and sources. Finally, to test whether the spectrolaminar motif consistently aligns with specific anatomical layers, we used electrolytic lesions to label the anatomical locations of key spectrolaminar landmarks. Histological analyses revealed that these landmarks mapped onto the same anatomical layers across recordings and cortical areas: the peak gamma power was located in layers 2/3, the peak alpha-beta power in layers 5/6, and the cross-over between relative gamma and alpha-beta power in layer 4.

Results

The aim of this study was to investigate whether in the primate cerebral cortex, oscillatory neuronal activity represented in the LFPs differs between layers, and if so, whether the laminar activity pattern is unique to each area or is preserved across cortical areas and represents a canonical property of all the cortex. We analyzed LFPs from intracortical electrophysiological recordings performed in multiple cortical areas of rhesus macaque monkeys (*Macaca mulatta*) using multicontact laminar probes (16, 24, or 32 contacts). We combined data from six cortical areas collected in two independent studies performed in different labs by different authors. Additional data was also collected from six other areas. The twelve areas in the combined dataset varied broadly in their anatomical and hierarchical position along the visual processing stream, ranging from V1 to LPFC (Fig. 1a). The probes were positioned with guidance from structural Magnetic Resonance Imaging (MRI) so that the contacts (i.e., recording channels) traversed all cortical layers as perpendicularly to the cortical sheet as was possible given the orientation of each cortical area with respect to of the recording chambers (Figure 1b,c). The relative position of each probe's channels with respect to the cortex was also confirmed by assessing the presence of multiunit activity. The two studies used different behavioral tasks with some similarities (see Methods). In both tasks, trials began with a period of gaze fixation followed by a visual stimulation period (presentation of a static picture in study one and a moving random dot surface in study two). Our analyses were applied to signals collected in the fixation and sensory stimulation periods.

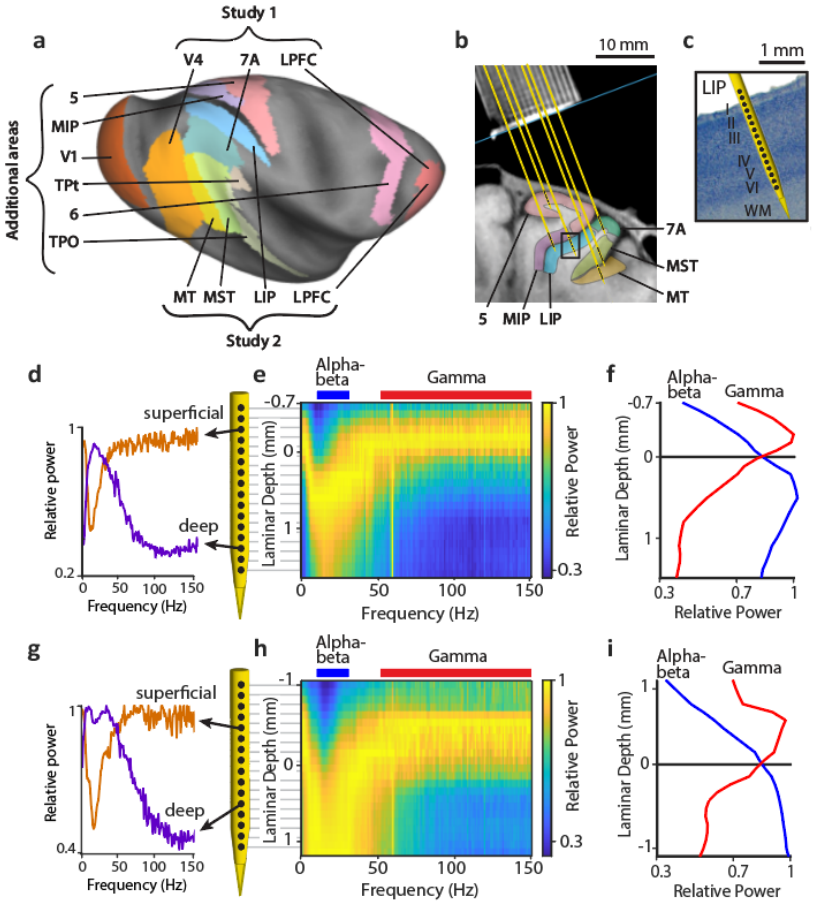

Figure 1. Laminar recording methods and laminar differences in LFP oscillatory power
(A) Inflated cortical surface of the macaque brain showing cortical areas recorded. (B) Structural MRI nearly-coronal section of one monkey from study 2 showing recording chamber grid (top) and location of areas MT, MST, 7A, LIP, MIP, and 5 on the right hemisphere. Red lines show the locations of example probes in all areas. (C) Nissl section from the same monkey corresponding to a 10x magnification of the black rectangular region in (B) with an example probe diagram showing the locations of recording channels (black dots) with respect to the cortical layers in area LIP. (d,g) Relative power as a function of frequency in a superficial layer channel and a deep layer channel from two example probes in areas LIP (d) and MT (g). (e,h) Relative power maps across channels for the two example probes. (f,i) Relative power averaged in the alpha-beta (blue) and gamma (red) frequency bands as a function of laminar depth for the two example probes.

Spectrolaminar pattern of relative LFP power in the macaque cortex

To compare the oscillatory activity of the LFP signals between cortical layers recorded by each probe, we obtained for each channel the mean LFP power spectrum across trials during the fixation and sensory stimulation periods of the task; at each frequency, we then divided the power of each channel by that of the channel with the highest power. The resulting relative power spectrum of individual channels revealed a common pattern across probes: oscillatory activity in higher frequencies (gamma, 50 – 150 Hz) had higher power in superficial channels than deep ones,

whereas oscillatory activity in the alpha-beta frequencies (10 - 30 Hz) had higher power in deep channels than superficial ones (Fig. 1d,g). This observation suggested the possibility that the relative power of each frequency varies smoothly across cortical layers, forming a distinctive spectrolaminar pattern that might be preserved across all cortical areas. To examine this, we stacked the relative power spectra of all channels in each probe to create a two-dimensional frequency-by-depth matrix of relative power values with a size of 150 1-Hz bins by 32 channels, referred to as the relative power map (Fig. 1e,h; see Methods).

The relative power maps confirmed a smoothly-varying transition of relative power across channel depths and frequencies, forming a characteristic "swoosh" pattern in which the peak relative power (yellow tones in Fig. 1e,h) shifted from superficial channels at delta-theta frequencies (1 – 6 Hz) to deep channels at alpha-beta frequencies and back to superficial channels at gamma frequencies. This pattern was present in probe recordings from all areas. To better examine how power at different frequency bands varies across layers, we averaged the relative power across the delta-theta, alpha-beta and gamma bands as a function of depth. We found an increasing deep-to-superficial gradient of gamma power peaking in superficial channels, and an increasing superficial-to-deep alpha-beta power gradient peaking in deep channels (Fig. 1f,i). An increasing deep-to-superficial gradient of power in the delta-theta frequencies was also present, although less consistently and less prominently (Supplementary Fig. 1a,b).

One of the most common characteristics across probe recordings in all recorded areas was the superficial-to-deep increasing alpha-beta power and decreasing gamma power gradients, and the cross-over between them (Fig. 1f,i). The cross-over point is the position at which the relative power of alpha/beta and gamma are equal. To examine how consistent the spectrolaminar pattern was across individual probes in each area, we aligned the relative power maps of all individual probes by the alpha-beta/gamma cross-over channel, and averaged the relative power maps across probes for each cortical area in each monkey and each study (Fig. 2). All average relative power maps showed the presence of the same spectrolaminar pattern that was visible in the individual example probe maps, characterized by higher gamma power (and to a lesser extent, delta-theta power, Supplementary Fig. 1c,d) in superficial channels than deep ones, and higher alpha-beta power in deep channels than superficial ones. That the spectrolaminar pattern is clearly visible in the average relative power maps, and that these maps are similar between areas, monkeys, and studies, strongly suggest that the pattern is a ubiquitous property across all cortex. To further confirm this ubiquity, we performed additional recordings in a variety of other cortical areas, including primary visual cortex (V1), somatosensory cortex (area 5), premotor cortex (area 6), auditory cortex (TPt), polysensory area TPO, and polysensory/somatomotor area MIP, and found that the spectrolaminar pattern was present in all these areas (Supplementary Fig. 2).

We then examined how robust the spectrolaminar pattern was to various recording and analysis conditions. First, in recordings made during probe insertion, we showed that the spectrolaminar pattern was apparent as a probe entered, traversed, and exited the cortical sheets, and the relative position and orientation of the pattern were indicative of the probe's location with respect to the cortex (Supplementary Fig. 3). Second, we showed that the spectrolaminar pattern was reliably identified in as few as 2 trials, corresponding to a 2-s recording (Supplementary Fig. 4). Third, we showed that the spectrolaminar pattern was observed both in the presence or absence of sensory stimulation, i.e., during the inter-trial interval and cue stimulus presentation task periods,

respectively (Supplementary Fig. 5). This indicates that the spectrolaminar pattern represents a basal cortical state.

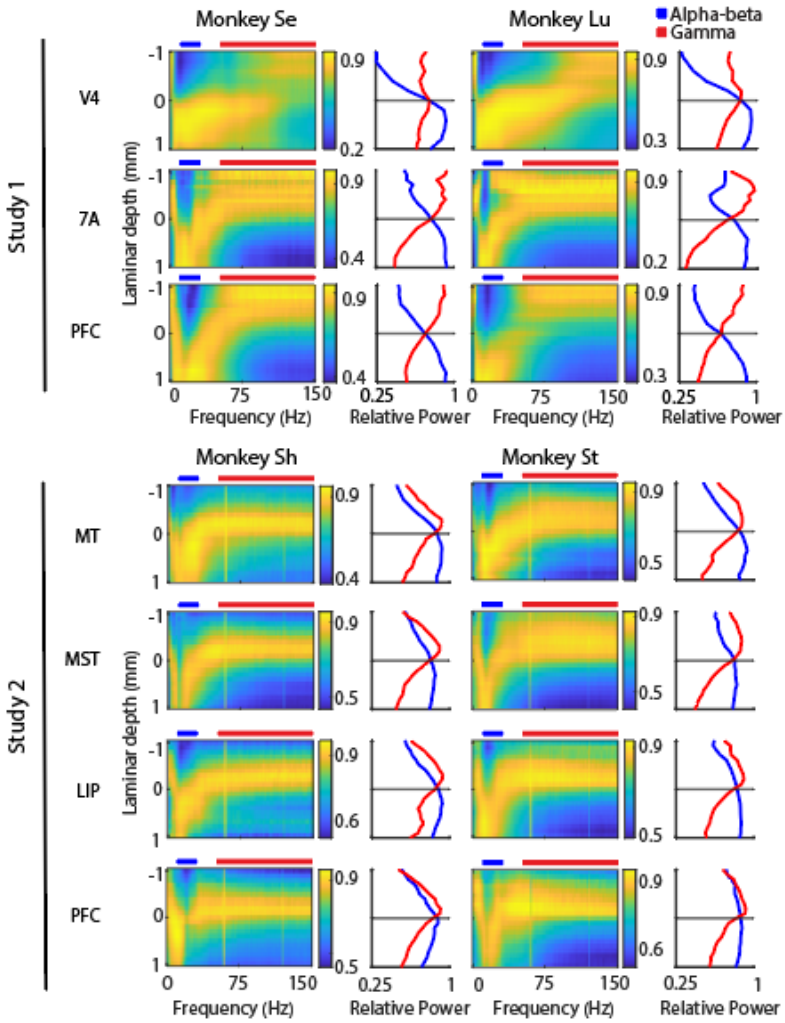

Figure 2 | The spectrolaminar pattern is ubiquitous across areas, monkeys, and studies
For each cortical area in each monkey and each study, across-probes average relative power map (left) and average relative power in the alpha-beta (blue) and gamma (red) bands as a function of laminar depth with respect to the alpha-beta / gamma cross-over channel.

Spectrolaminar pattern is preserved across cortical areas, monkeys, and studies

To quantify the degree of similarity between the relative power maps of probes recorded within or between cortical areas, monkeys, and studies, we expressed each relative power map as a bidimensional frequency-by-depth image, and applied image similarity (IS) analysis – an image-computable metric that quantifies the similarity between two images from zero (most dissimilar) to one (identical) [35]. We grouped probes by cortical area, and for each pair of areas within and between monkeys / studies, we obtained the IS value comparing the across-probes mean relative power maps within or between groups using a randomized probe sub-grouping procedure (see Methods). Last, using a channel randomization procedure, we computed the laminar IS – an

estimate of the image similarity that is accounted for by the laminar structure of the relative power maps, and determined whether the laminar IS was significantly higher than expected by chance.

Figures 3a-d show the laminar IS comparing probe relative power maps within and between cortical areas and monkeys in each study. Significant laminar IS was present across all these comparisons ($P < 0.05$, corrected for multiple comparisons), indicating quantitatively that the spectrolaminar pattern of relative LFP power is preserved across cortical areas and monkeys. Next, to examine whether the spectrolaminar pattern was also preserved across recordings from the two independent studies, we computed laminar IS comparing relative power maps between cortical areas across the two studies (Fig. 3e). For all comparisons, there was significant laminar IS (paired t-tests, $P < 0.05$, corrected for multiple comparisons), although they were lower than the IS values obtained within each study. The similarity in the relative power maps obtained in different monkeys and studies, despite methodological differences between the two studies, demonstrates the robustness of the spectrolaminar pattern of LPF power.

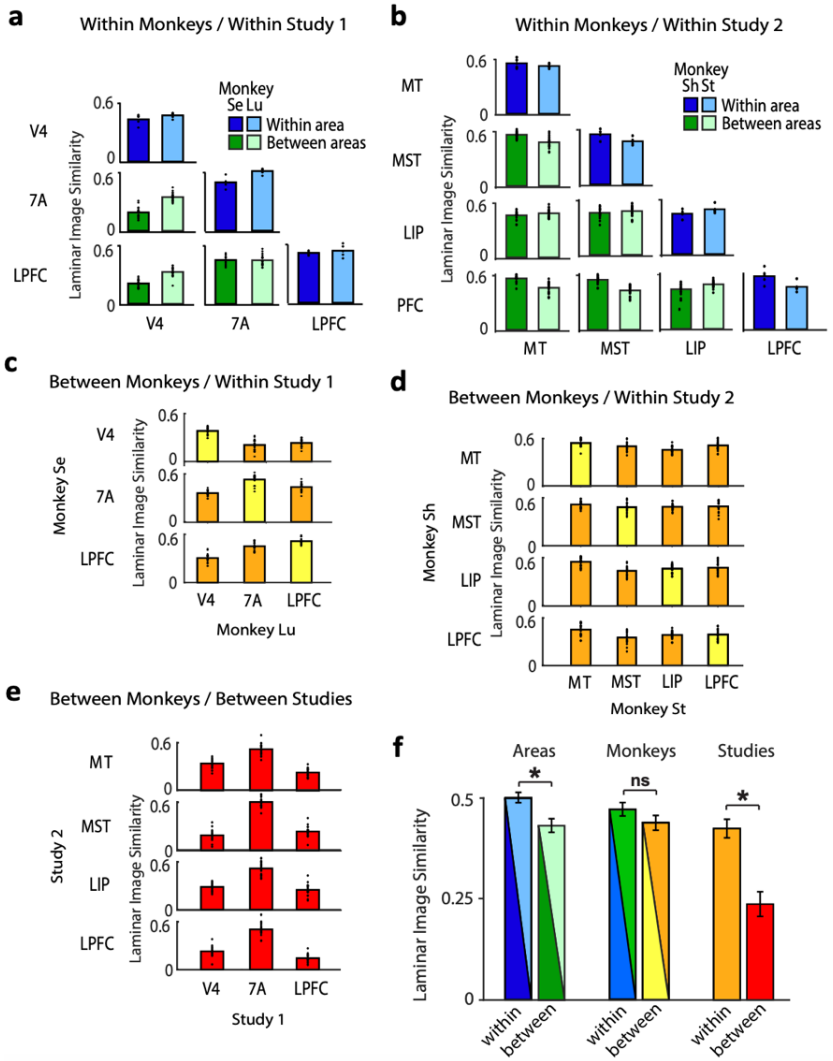

Figure 3. Similarity between relative power maps within and between cortical areas, monkeys and studies.

(a,b) Mean laminar image similarity of relative power maps across probe recordings within (blue) and between (green) areas within each monkey within Study 1 (a) and Study 2 (b). (c,d) Mean Laminar image similarity within (yellow) and between (orange) areas between monkeys within Study 1 (c) and Study 2 (d). (e) Mean laminar image similarity between areas, between monkeys and between studies. (A-E) The height of each bar corresponds to the Mean laminar image similarity across all randomized probe splits (individual dots; see Methods). (F) Mean Laminar image similarity across all comparisons within- and between- areas, monkeys and studies. Mean +/- SEM across all (independent) comparisons are shown. The colors of the bars represent the colors of the individual comparisons in (A-E) that were averaged.

While all cortical areas share a common anatomical laminar motif, it is well known that this motif shows some variations that are unique to each area. Therefore, we considered the possibility that besides the observed similarity in the spectrolaminar pattern across all cortical areas, the pattern in each area may show some unique variations that distinguish it from other areas. To assess this, we compared the laminar IS values of relative power maps recorded within and between different areas within monkeys. We found that mean laminar IS across all within-area comparisons was significantly higher than that across between-area comparisons (Fig. 3a,b,f; unpaired *t*-test, $P = 0.006$). This suggests that despite the similarity in the spectrolaminar pattern between cortical areas, each area differs from others to a small degree. Next, we compared the similarity of relative power maps recorded from the same monkey vs. from different monkeys, and found no significant difference (Fig. 3f; unpaired *t*-tests, $P = 0.18$). This suggests that the spectrolaminar pattern is consistent across individual monkeys, and that inter-individual differences are only minor. Last, we found that the similarity of relative power maps recorded within each study was significantly higher than between studies (Fig. 3f; unpaired *t*-test, $P < 0.001$, respectively). Thus, despite the generalization of the spectrolaminar patterns across studies, the patterns are most similar when recorded by the same study. This may be due to differences in electrophysiological methods between both studies.

Current Source Density pattern is less preserved than spectrolaminar pattern of relative power

Our observation that the spectrolaminar pattern of relative LFP power is preserved across cortical areas and monkeys in data collected in different studies suggests that this pattern may represent the most robust and ubiquitous physiological signature of the six-layer anatomical motif of the cortex known to date. It is well established that there is one other pattern of neural activity known to map onto the cortical laminar architecture: Current Source Density (CSD, [20]). CSD shows the temporal dynamics of laminar current sources and sinks following sensory input. In visual cortical areas, numerous studies have shown that following visual stimulation, a current sink first occurs approximately in layer IV and then travels towards more superficial and deeper layers [20,21,36–39]. Because this appears to be a common phenomenon across visual cortical areas, CSD has been widely used as the only method to date to estimate the location of cortical layers in laminar electrophysiological recordings: the early current sink is used to estimate the location of layer IV. This raises several important questions: Which of the two laminar patterns of activity – CSD or the spectrolaminar pattern of relative power – is more ubiquitous across the cortex? Second, which pattern maps more accurately onto the laminar anatomical cortical motif? Third, which pattern

serves as a better method for estimating the anatomical location of laminar electrophysiological recordings?

To address these questions, we obtained CSD as a function of time and channel depth for each probe in the datasets of Studies 1 and 2 and estimated the channel at which the early sink occurred following the onset of the stimulation period of the task. Combining monkeys, areas, and studies, our total dataset consisted of 942 probes. Of these, a clearly identifiable early CSD sink (see Methods) was present in 43.8% of the probes (413). In contrast, a clear pattern of alpha-beta/gamma relative power cross-over was identifiable in 48.1% of the probes (453), a significantly higher percentage than for the early CSD sink (Chi-squared test, $P < 0.0001$). This suggests that the spectrolaminar pattern is more robust across the cortex than the CSD pattern. In a subset of 298 probes, both the alpha-beta/gamma cross-over and CSD sink were identifiable. For all subsequent CSD analyses, we only used probes that showed an early CSD sink.

Among probes showing an identifiable early CSD sink, we next examined how preserved the CSD pattern was within and between cortical areas, monkeys, and studies. For each probe recording showing a clearly identifiable CSD sink, we centered the CSD time-by-depth map at the early sink channel. We then averaged all probe CSD maps from each cortical area for each monkey in each study. While the CSD early sink was visible in the average CSD maps of all areas, the characteristics of the early sink, including duration, intensity and laminar thickness, appeared to vary drastically between areas, monkeys, and studies, as did other components of the CSD pattern at various depths (Fig. 4a,b). This suggested that the CSD pattern was more dissimilar between cortical areas, monkeys, and studies than the spectrolaminar pattern of relative power.

To quantify the similarity of the laminar patterns of CSD sinks and sources within and between cortical areas, monkeys, and studies, we compared their two-dimensional time-by-depth CSD maps using the same Image Similarity analysis method described for the relative power maps (see Methods). Overall, we found that the laminar IS values for the above comparisons of CSD maps (Supplementary Fig. 6), were largely reduced compared to those from the comparisons of relative power maps (Fig. 3). In addition, 81% all CSD map comparisons between cortical areas, monkeys, and studies, showed non-significant laminar IS values, whereas for relative power maps, all comparisons showed significant laminar IS. Lastly, we examined the extent to which the CSD pattern generalized across cortical areas, monkeys, and studies. For areas, the average laminar IS across between-groups comparisons was significantly lower than across within-group comparisons (Fig. 4C; unpaired t-test, $P = 0.017$). Laminar IS values comparing between- vs. within- monkeys and studies were not significantly different (Fig. 4c; unpaired t-test, monkeys: $P = 0.10$, studies: $P = 0.78$). The average laminar IS values across all between-areas, between-monkeys, and between-studies comparisons were close to 0. These results indicate that the CSD pattern did not robustly generalize between areas or monkeys.

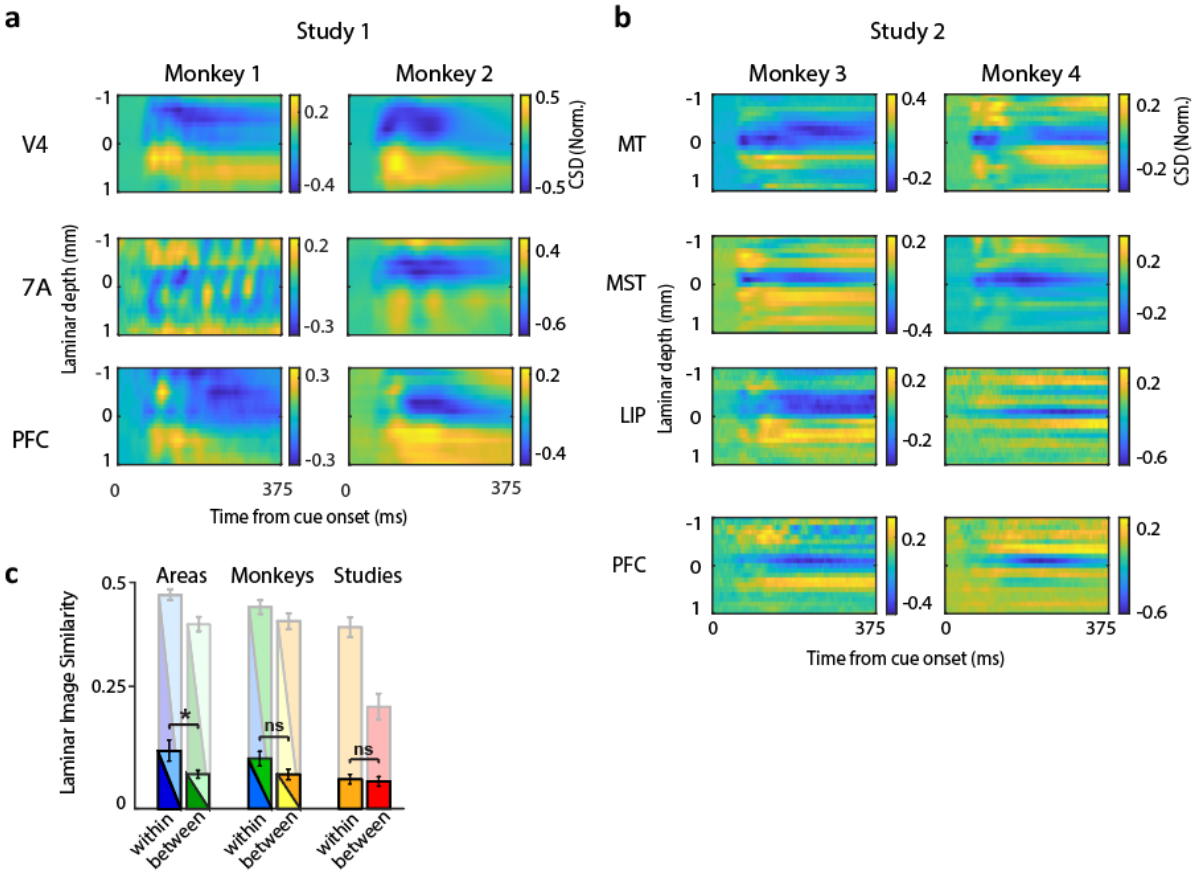

Figure 4. Comparison of current source density (CSD) laminar patterns between cortical areas, monkeys, and studies.
(a,b) Average CSD maps across probes from each area and monkey in Study 1 (a) and Study 2 (b). Current sinks are negative (blue), sources are positive (yellow). CSD values have been normalized by the peak negative value. Laminar position zero (y-axis) is the position of the first identifiable current sink. (c) Full color bars indicate the average laminar image similarity for within- vs. between monkeys (purple and blue bars), within- vs. between monkeys (dark blue and green bars), and within- vs. between studies (green and red bars). Opaque colors are the same comparisons for power. Mean +/- SEM are indicated across independent comparisons. Stars indicate significance at a level of $P < 0.05$, paired t-test.

Spectrolaminar pattern in V1

By showing the similarity in the spectrolaminar pattern between multiple cortical areas at a variety of visual processing stages, ranging from V4/MT to LPFC, our results suggest that the spectrolaminar pattern is ubiquitous across cortical areas. However, previous studies have shown that the laminar architecture of certain areas such as V1 displays distinctive histological characteristics that differ largely from those in most other cortical areas[40]. Indeed, the anatomical organization of V1 has the most striking lamination patterns of any cortical area (e.g., possessing sub-layer within layer 4 for magnocellular and parvocellular thalamic inputs). We thus investigated

whether the observed spectrolaminar pattern is preserved even in a distinctive area such as V1. Using similar methods as already described (Fig. 1a), we performed additional laminar electrophysiological recordings in area V1 of one monkey. Data were collected in a different monkey and lab (Maier Lab) than the previous data.

We found that the relative power maps in V1 showed a spectrolaminar pattern that was consistent with that in other areas: superficial channels had higher LFP power in the gamma frequencies than deeper channels, whereas deeper channels had higher LFP power in the alpha-beta frequencies than superficial channels (Fig. 5a,b). We next tested if the pattern in V1 generalizes to other areas. To do this, we computed a global laminar IS value, defined as the laminar IS values between a given area and every other area. We found that the global laminar IS values were very similar between most areas (Fig. 5c). and that those in V1 were not significantly different from any other area (unpaired t-tests, corrected for multiple comparisons) These results indicate that despite the distinctive laminar architecture of V1 compared to other areas, its resulting spectrolaminar pattern does not particularly diverge from those of other areas. We next performed a comparable analysis to determine whether the laminar pattern of CSD sources and sinks in V1 (Fig. 5d) is similar to that of other areas. Once again, global laminar IS of V1 to other areas was not significantly difference from global laminar IS of any other areas (Fig. 5e).

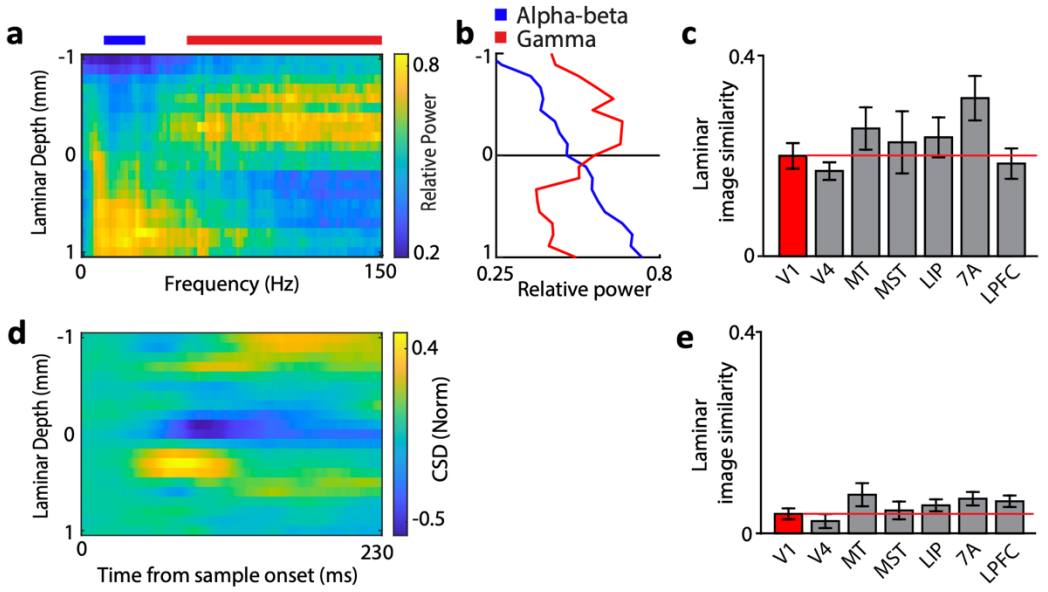

Figure 5. V1 spectrolaminar pattern and CSD and their similarity with other cortical areas
(a) Average spectrolaminar pattern recorded in area V1. The zero point on the y axes corresponds to the gamma to alpha/beta cross-over channel of each individual probe (N = 10). (b) The average relative gamma power (50-150 Hz, red lines) and alpha-beta power (10-30 Hz, blue lines). (c) Global laminar image similarity values between each area in turn and all other areas. The red horizontal line is the height of the V1 bar, for comparison. Mean +/- SEM. (d) The average current source density map for area V1. Time 0 is the onset of a visual stimulus. Current sinks are negative (blue), sources are positive (yellow). Current source density units have been scaled so that the peak negative value is -1 on each session. Laminar position zero (y-axis) is the position of the first identifiable current sink. (e) Same as (c), but for CSD.

Histological mapping of spectrolaminar pattern and CSD

Having established that the spectrolaminar pattern could be identified in areas V1, V4, MT, MST, LIP, 7A, and LPFC, we hypothesized that the spectrolaminar pattern was anchored to specific layers that was consistent across probes. Alternatively, it could be that the spectrolaminar pattern is present in each area but given the laminar variation across cortex, does not clearly correspond to specific layers. To test this, we parametrized the spectrolaminar pattern using three markers: the probe channel having the largest relative power in the gamma frequency range, alpha-beta frequency range, and the channel at which the relative power of gamma and alpha-beta was equal (referred to as the "cross-over"). For comparison, we parameterized the CSD with a single parameter, the channel location of the first detectable current sink.

For a subset of areas (LIP, PFC, MST, V1, and premotor cortex area 6), we performed additional electrophysiological recording sessions during which we created electrolytic markers to precisely reconstruct the probe's location in histological sections (N = 8 probe locations in LIP, N = 10 probe locations in LPFC, N= 2 probe locations in MST, N = 5 probe locations in V1, N = 1 location in premotor cortex, see Methods for details). We subsequently extracted the brain and performed histology. Example Nissl stains from two recording sessions in areas LIP and LPFC containing electrolytic markers are shown in Fig. 6a and b. The electrolytic marker can be identified in the Nissl section as a circular spot darker than the surrounding tissue. The locations of all channels in the probe were then reconstructed relative to the electrolytic marker by accounting for the known inter-channel spacing and tissue shrinkage due to histological processing (see Methods). The colored dots correspond to the channel with highest gamma power (in red) and alpha-beta power (in blue), and the cross-over channel (in green). In both examples, the channel with highest gamma power was in layer 3, the channel with highest alpha-beta power in layer 5, and the cross-over was in layer 4 or the layer 4-to-5 boundary. Supplementary Fig. 7 shows each individual probe reconstruction with physiological and laminar landmarks in LIP and LPFC. Probe reconstructions with histology for areas with fewer data points (V1, MST, premotor) are shown in Supplementary Fig. 8. The locations of gamma in superficial and alpha/beta in deep layers was largely consistent for these areas, but V1 alpha/beta was an exception. V1 had the highest alpha/beta power in white matter channels.

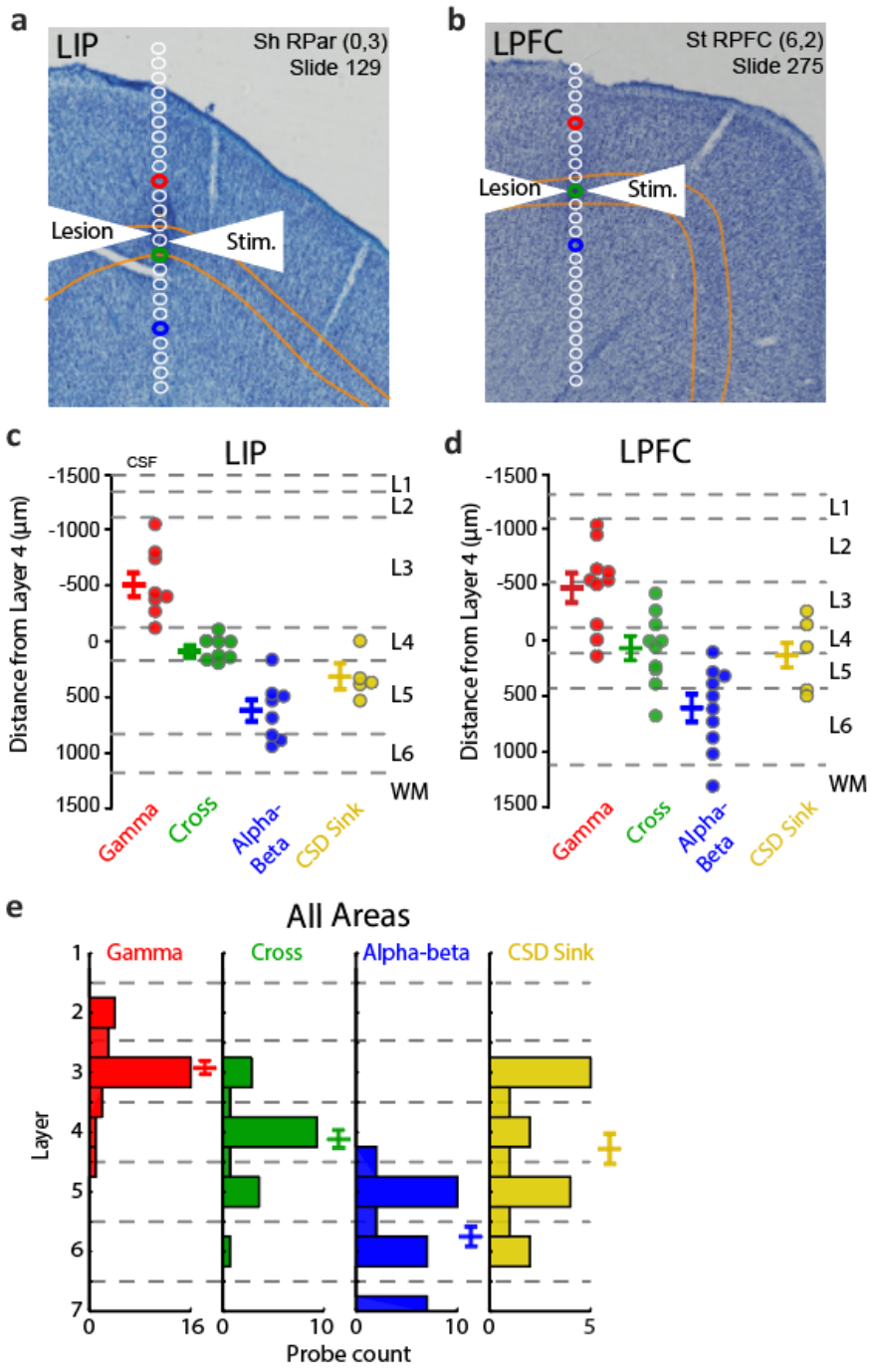

Figure 6. Histological mapping of spectrolaminar pattern of relative LFP power with respect to anatomical layers

(a) An example histological Nissl-stained section in area LIP in monkey Sh showing a clear electrolytic lesion (dark spot, see white arrows). Reconstructed probe channels are shown in white. The laminar position of layer 4 is outlined in yellow. The red, green, and blue dots correspond to the channel with highest gamma power, the gamma/beta cross, and the channel with highest beta power on the probe. (b) Same as (a), but for area LPFC in monkey St. (c) For each independent probe, we performed probe reconstructions shown in (a) and (a) and then measured the distance from each physiological landmark to the center of layer 4 in micrometers. Each dot is an

independent probe. The mean and standard errors are indicated with horizontal colored lines. Black dotted lines indicate the mean laminar boundaries for that area. (d) Same as (c), but for area LPFC. (e) Histograms of the layers where the four physiological measures were found across all available data (LIP, LPFC, MST, and V1). Mean +/- SEM are indicated with horizontal colored lines.

To quantify these results and test their robustness, we measured the distance of each physiological marker to the center of layer 4 in micrometers. Negative values indicate the physiological marker was more superficial than layer 4. Positive numbers indicate the physiological marker was deeper than layer 4. The results are shown in Figure 6c,d. Each dot indicates independent measurements from separate probes. The mean distance of the gamma peak to layer 4 was – 529um for LIP and -488um for PFC (95% CI, [-328um, -730um] for LIP, [-247, -729um] for PFC). The mean distance of the alpha-beta peak to layer 4 was +628 um for LIP and +693um for PFC (95% CI, [+459um, +797um] for LIP, [+457um, +930um] for LPFC). The mean distance of the cross-over channel to layer 4 was -77 um for LIP and -34um for PFC (95% CI, [-7um, -161um] for LIP, [-186um, -255um] for PFC).

These measured distances to the middle of layer 4 could in principle correspond to different layers because layer thickness across cortex is variable[41]. Therefore, we reconstructed the physiological markers for each probe and quantified the average layer at which they were observed. If markers were observed at a border between layers they were counted as a value of 0.5 away from the layer center. For example, a physiological marker at the border between layers 2 and 3 was given a value of 2.5. We performed this analysis after collecting all available data from LIP, LPFC, MST, and V1. The mean laminar position of the gamma peak was 2.9 (N=27, 95% CI, [2.8, 3.0]), gamma/beta cross was 4.12 (N = 25, 95% CI, [4.0, 4.3]), and alpha/beta peak was 5.8 (N = 28, 95% CI, [5.6, 6.0]). The mean laminar position of the early CSD sink was 4.3 (N = 16, 95% CI, [4.0, 4.6]). The variability of the gamma power peak was significantly lower than both the CSD sink (Bartlett's test for unequal variances, P=0.0026) and the alpha/beta power peak (Bartlett's test for unequal variances, P=0.03). The variability of the gamma/beta cross trended towards being lower than the CSD sink (Bartlett's test for unequal variances, P=0.07).

Discussion

A ubiquitous spectrolaminar pattern across the cortex

In summary, we report the existence of a spectrolaminar pattern in the macaque cortex consisting of a combination of frequency-specific LFP power gradients across cortical layers. Using electrolytic markers and histological techniques to identify the precise location of these gradients with respect to the anatomical layers, we determined that the peak of gamma power is located in superficial layers 2/3, the peak of alpha-beta power is in deep layers 5/6, and the crossover point between the gamma and alpha-beta power gradients is in layer 4.

We further showed that this spectrolaminar motif is preserved in all cortical areas studied, suggesting that it is a ubiquitous property of the cortex. Future studies in various other cortical areas will help corroborate this. We showed that spectrolaminar patterns were more similar within

each area than between areas. This supports the idea that each area is constructed as a specific variation around a common theme and raises the important question as to whether and how these variations contribute to the functional specialization of each area. Evidence of systematic inter-areal variations comes from a recent study in which the peak frequency of theta, beta, and gamma were observed to increase as the cortical hierarchy ascended from visual to parietal to prefrontal cortex [42].

Given that the spectrolaminar pattern mapped onto the laminar anatomy, it is reasonable to hypothesize that it is not unique to the macaque brain, but instead is preserved across mammalian species with a six-layered cortex. Supporting this, laminar recordings from marmoset monkeys [33] and rats [18,26] have shown gradients of gamma and alpha-beta power across layers that seem consistent with the spectrolaminar motif. Laminar reconstructions in magnetoencephalographic recordings [43] and simultaneous laminar fMRI-EEG recordings [44] have provided some evidence that this motif is also present in the human cortex. Analyses of laminar cortical recordings in a broader variety of animal models will be necessary to confirm the ubiquity of the spectrolaminar motif across mammals, and may provide insights into its evolutionary origins.

Mechanisms and functions of the spectrolaminar pattern

The precise neuronal mechanisms that generate the different oscillatory components of the spectrolaminar pattern, such as higher superficial gamma power and higher deep alpha-beta power, remain unknown. One possibility is that there is an epicenter for the generation of gamma rhythms (and perhaps also theta) in superficial layers. In addition, there may be a generative mechanism for beta rhythms in deep layers [26] or in the interactions between deep and superficial layers [10,11,31,45]. Supporting this idea, previous studies in cortical slice preparations from rats have shown evidence for the origins of gamma oscillations in layer 3 [46] and beta oscillations in layer 5 [26,47] or in the interactions between superficial and deep layers (Roopun et al., 2008). Whether these mechanisms are also present *in vivo* and are preserved in macaques and other mammals remains to be examined. Another possibility is that the deep layer beta is a feature of the filtering property of the dendrites of deep layer cells which extend their apical dendrites into superficial layers. This would be consistent with recent observations that beta current sinks are strongest in superficial layers but exert their strongest effect on spiking in deep layers [48].

The notion that the spectrolaminar motif is a ubiquitous property of the cortex has important theoretical implications for understanding the fundamental principles of cortical structure and function. It has been proposed that the six-layer cortical anatomical motif is designed to enable a canonical microcircuit with versatile computational capabilities [4,7]. For each area to accomplish its functional specialization, it would develop a distinct variation of this anatomical theme, in addition to its specific connectivity with other cortical and subcortical areas. The concept of a laminar theme-and-variations in the cortex is readily apparent at the anatomical level by the observation that cortex contains six layers with some variations in their thickness and properties [9]. However, it has been much more difficult to identify themes and variations in electrophysiological activity patterns of the cortex.

The pattern of CSD sinks and sources remained for decades as the only known activity pattern reflective of the laminar motif and the canonical microcircuit, revealing a characteristic sequence

of current flows through the layers of the microcircuit. The spectrolaminar pattern is now the second known functional correlate of the laminar anatomical motif; importantly, this suggests that the canonical microcircuit also works via layer-specific neuronal oscillations, and that such oscillatory mechanisms play a fundamental role in the function of all cortical areas. Laminar differences in the frequency composition of the LFPs have been previously shown to cause differential entrainment of local spiking activity [12] and create separate frequency channels for feedforward communication (using theta and gamma frequencies in superficial layers) and feedback communication (using alpha-beta frequencies in deep layers; [30,32]. Anatomically, superficial layers provide the strongest feedforward cortico-cortical output and deep layers provide the strongest feedback cortico-cortical output [49,50]. Thus, it is possible that superficial vs. deep layers form separate compartments along cortex [37], serving the distinct functions of feedforward and feedback processing, respectively [5,51].

Frequency-based layer identification procedure (FLIP)

Taking advantage that the spectrolaminar pattern accurately maps onto histologically-identified cortical layers and is highly preserved across cortical areas, monkeys and studies from different labs, we developed FLIP – a Frequency-based Layer Identification Procedure. FLIP allows experimenters to easily map the location of all channels in a linear probe with respect to the cortical layers during electrophysiological recordings. Experimenters first compute the normalized gamma and alpha-beta power of all channels following the procedure described in our methods. The channels containing the peak alpha-beta power, the peak gamma power, and the alpha-beta/gamma cross-over point are then used as estimates of the locations of layers 2/3, 5/6, and 4, respectively (see Methods). All other channels are then mapped with reference to those three anatomical landmarks.

Until now, CSD was the only available method for laminar identification in electrophysiological recordings. Our results show that FLIP offers many advantages as an alternative to CSD. First, the functional landmarks in the spectrolaminar pattern are identifiable in a higher percentage of probe recordings than the CSD early sink. Second, FLIP is more generalizable and consistent across cortical areas, monkeys, and studies than CSD. Third, our histological mapping indicated that layer 4 can be more accurately identified by the alpha-beta/gamma cross-over than by the CSD early sink. Fourth, compared to the CSD early sink, the spectrolaminar motif spans more layers and contains more functional reference landmarks (gamma peak, alpha-beta peak and alpha-beta/gamma cross-over). Fifth, due to its low signal-to-noise ratio, CSD typically requires multiple trials of repeated stimulation in the specific sensory modality that optimally drives each cortical area. In contrast, the spectrolaminar pattern can be robustly identified in as little as 2-5 s of data (Supplementary Fig. 4) collected with or without sensory stimulation (Supplementary Fig. 5). Fifth, while CSD requires the user to manually identify the early sink, FLIP is fully automated and thus considerably reduces the duration of data analysis, especially in large datasets. In the future, it may be possible to improve the accuracy of layer localization methods by combining complementary laminar information from spectrolaminar, CSD, and neuronal spiking patterns using machine learning approaches. It remains to be examined whether the temporal dynamics of the spectrolaminar patterns, such as changes from resting state to sensory stimulation (Supplementary Fig. 5), may convey additional laminar information.

The fact that FLIP is fully automated and fast to perform opens the doors for the development of several applications. By continuously determining a probe's location with respect to cortical layers in close-to-real time, FLIP could be used to guide probe placement during acute or chronic implantation (Supplementary Fig. 3). Moreover, probe placement could become fully automated and unsupervised by allowing the output of FLIP to perform closed-loop control of a standard computerized microdrive with the help of structural MRI data. In medicine, these methods may improve surgical implantation of probes in patients with epilepsy (for pre-surgical screening [52], Parkinson's (for deep brain stimulation [53], and paralysis (for brain-machine interface systems, [54], among others. Lastly, some neurological and psychiatric disorders are associated with abnormal beta oscillatory patterns in Parkinson's [55] and abnormal gamma oscillatory activity schizophrenia [56,57] and Alzheimer's disease [58]. If these abnormalities result in atypical spectrolaminar patterns, measuring such patterns may help in diagnosing, understanding, and eventually treating these disorders.

A spectrolaminar framework for cortical electrophysiology

To understand the fundamental computational principles of the cortex, it will be necessary to transcend the current approach where each cortical area is studied in isolation and move towards a collective approach where the results of all studies are easily integrated and compared. We believe that the long-term goal should be to build a generalized cortical theory that explains how it is possible for all cortical areas to accomplish a wide variety of functions via minor variations of the same theme – the canonical microcircuit. Given the laminar nature of this microcircuit, it will be crucial to establish laminar cortical electrophysiology as a new gold standard. This is now easier than ever, since laminar probes have recently become increasingly accessible, affordable, higher-quality, and are fabricated with increasing density and number of channels [59].

One longstanding limitation in primate studies is that the cortex has been almost exclusively investigated either anatomically – through histological analyses of cortical layers in post-mortem tissue – but without access to neuronal activity, or electrophysiologically – by recording neuronal activity in behaving animals – but without access to the anatomical laminar location of the recorded neurons. The ubiquity of the spectrolaminar pattern offers a unique opportunity to establish a laminar approach to investigating cortical function that is standardized across areas and studies and that bridges the anatomical and electrophysiological approaches. To this end, we propose a spectrolaminar framework for cortical electrophysiology. By applying FLIP, the electrophysiological signals obtained from all the channels of each probe can be mapped onto spectrolaminar space. This same space is then used to map all the results of a study. Furthermore, population results are presented not only classified into cortical areas – as most studies have done to date, but also by cortical layers within each area. The spectrolaminar framework will allow all studies of the cortex to use a common anatomical laminar reference, as well as a common functional reference in the frequency domain, facilitating comparisons between studies within and across cortical areas. This collective approach will lead to a better understanding of the different roles of individual layers in the computations and functions of the cortex, and help identify similarities in these laminar roles across cortical areas. These similarities will be key to unraveling the mechanistic principles of the canonical microcircuit across the cortex.

Methods

Experimental Model and Subject Details

Five adult rhesus macaques (*macaca mulatta*) were used in this study. Study 1 used two female monkeys, monkey Se (6 years old and 5.0 kg) and monkey Lu (17 years old and 10.5 kg). In study 2 we used two male monkeys, Monkey Sh (9 years old and 13.7 kg) and monkey St (10 years old and 12.1 kg). Recordings in area V1 were performed in one male monkey (Monkey Bo 14 years old and 7.5 kg). The animals were housed on 12-hr day/night cycles and maintained in a temperature-controlled environment (80°F). All procedures were approved by the MIT/Vanderbilt IACUC and followed the guidelines of the MIT/Vanderbilt Animal Care and Use Committee and the US National Institutes of Health.

Electrophysiological Recordings

Behavioral Training and Task

Monkeys were trained to sit in a primate chair inside a sound-attenuating behavioral testing booth. Monkeys Se and Lu (Study 1) were seated 50 cm away from a 24-inch LCD monitor with 144 Hz refresh rate (ASUS, Taiwan). Monkeys Sh and St (Study 2) were seated 57 cm away from a 27-inch LCD monitor with 120 Hz refresh rate (Acer, Taiwan). Monkey Bo was seated 57 cm away from a 24-inch VIEWPixx /3D monitor with 120 Hz refresh rate. Eye tracking was performed using an Eyelink 1000 system at 1000 Hz sampling rate in Study 1, Eyelink 2 system at 500 Hz sampling rate in Study 2, and Eyelink 2 system at 1000 Hz sampling rate for the V1 study.

Using positive reinforcement, we trained monkeys to perform various tasks. For this study, we only analyzed data from the task periods prior and during the initial stimulus presentation; all other task details were irrelevant. Monkeys in studies 1 and 2 were trained to fixate a point at the center of the screen (fixation window radius: 2-3 visual degrees for monkeys Se, Lu; 2.6 for monkeys Sh and St) for a duration of 1s and were then presented a cue stimulus. The cue stimulus was a naturalistic image in Study 1 (chosen from 3 possible images) and a moving full-screen random dot surface in Study 2 (5 dots/deg^2; 0.15 deg dot diameter; 10.9deg/s dot speed). We used a screen flash in the V1 study. For the main power and current source density analysis, we used the times in the task that were consistent across studies: we analyzed the period from 500 ms pre-cue to 500 ms post-cue.

Electrophysiological Recordings

All of the data were recorded through Blackrock headstages (Blackrock Cereplex M, Salt Lake City, UT), sampled at 30 kHz, band-passed between 0.3 Hz and 7.5 kHz (1st order Butterworth high-pass and 3rd order Butterworth low-pass), and digitized at a 16-bit, 250 nV/bit. All LFPs were recorded with a low-pass 250 Hz Butterworth filter, sampled at 1 kHz, and AC-coupled.

In monkeys Se, Lu, St, and Sh, we implanted a custom-machined PEEK or Carbon PEEK chamber system with three recording wells. In monkeys Se and Lu, the recording chambers were placed over visual/temporal, parietal, and lateral prefrontal cortex. In monkeys St and Sh, three recording chambers were placed over right parietal cortex and left and right lateral prefrontal cortex; in both prefrontal chambers, we additionally performed a durotomy and implanted a transparent silicon-based artificial dura following procedures similar to those in Ruiz et al., 2013 [60]. The process for making the chambers was based on design principles outlined previously[61]. Monkey Bo was implanted with a 20mm chamber over V1 and affixed with dental acrylic and ceramic screws. For monkeys Se, Lu, St, and Sh, we obtained an anatomical MRI scan (0.5mm^3 voxel size) and/or CT scan to extract the bone and co-register the skull model with the brain tissue. We designed the center of each chamber to overlie the primary recording area of interest. Chambers for monkeys Se and Lu were additionally designed to have an optimal angle for perpendicular recordings relative to the cortical folding in areas V4, 7A, and LPFC. For monkeys St and Sh, two were designed to optimally cover LPFC (right and left cortical hemispheres, one chamber per hemisphere) and one to access LIP, MT, and MST at the most perpendicular angle possible (Fig. 1b). After the recording chambers were implanted, MRIs were taken with the recording grid in place, filled with water, which created a marker to co-register each possible probe trajectory with the animal's anatomy, and to confirm trajectories that were as close to perpendicular as possible.

We recorded a total of 213 sessions with laminar probes (Monkey Se: 38, Monkey Lu: 29, Monkey Sh: 54, Monkey St: 82, Monkey Bo: 10). In each session, we inserted between 1-6 laminar probes ("U probes" or "V probes" from Plexon, Dallas, TX) into each recording chamber with either 100, 150, or 200 um inter-site spacing and either 16, 24 or 32 total contacts/channels per probe. This gave a total linear sampling of 3.0 – 3.1 mm on each probe. For all monkeys the recording reference was the reinforcement tube, which made metallic contact with the entire length of the probe (total probe length from connector to tip ranged between 70 and 120 mm). When probes contained noisy channels (average power greater than 2 standard deviations above the mean of all channels, typically occurring in less than 5% of all channels), data for these channels were replaced with interpolations based on nearest neighbors prior to analysis.

Lowering procedure and laminar placement of probes

For monkeys Se and Lu, we first punctured the dura using a guide tube. Then we lowered the laminar probes through the guide tube using custom-built drives that advanced with a turn screw system (as previously described in[10,62]). In order to place the channels of the laminar probe uniformly through the cortex, spanning from surface through the gray matter to the white matter, we used a number of physiologic indicators to guide our probe placement, as previously described. First, the presence of a slow 1 – 2 Hz signal, a heartbeat artifact, was often found as we pierced the pia mater and just as we entered the gray matter. Second, as the first channels of the probe entered the gray matter, the magnitude of the local field potential increased, and single unit spiking activity and/or neural hash became apparent, both audibly and visually with spikes appearing in the online spike threshold crossing. Once the tip of the probe transitioned into the gray matter, it was lowered slowly an additional ~2.5mm. At this point, we retracted the probe by 200-400 um, and allowed the probe to settle for between one to two hours before recording. We left between 1-3 channels out of gray matter in the overlying Cerebral Spinal Fluid (CSF). We also used structural MRI-guidance to inform approximate insertion depth, and used the above criteria to finalize probe

placement. We used the same general probe insertion procedure in monkey Bo, except we used a custom-made drive from Narishige (Tokyo, Japan).

For monkeys St and Sh in Study 2, we used a similar probe insertion procedure, with the following differences. Probe insertion was controlled with an electronic Microdrive (NAN Instruments Ltd., Israel). The probe location was estimated by the Microdrive penetration depth with reference to structural MRI maps, and precise placement across the cortical sheet in the target area was guided by the appearance of distant and nearby multi-unit and single unit spiking activity across probe channels. We then waited for 30 minutes to one hour before recording to allow probes to settle.

Electrophysiological Data Analysis

Power Analysis

Power analysis was performed on 1 second time windows (500 ms pre-stimulus to 500 ms post-stimulus). The stimulus was either the cue stimulus onset (Study 1 and 2) or the flash stimulus (Study 3). Power analyses used the fieldtrip toolbox for Matlab[63]. We used the function ft_freqanalysis with method 'mtmfft'. This implements a multitaper spectral estimate[64]. We used 2 Hz smoothing in the spectral domain. Power was calculated on individual trials and then averaged across trials. We then obtained the relative power maps for each probe separately as follows:

$$Relative\ Power_{(c,f)} = \frac{Power_{(c,f)}}{\max\left[Power_{(1:nchan,f)}\right]}$$

Where c is each channel on the probe and f is each frequency from 0 – 150 Hz. For each probe this resulted in a 2-dimensional matrix, with channels on the y-axis and frequency on the x-axis. Thus at each frequency, every channel had an intensity between 0 and 1. Values of 1 indicate the channel that had the highest power at that frequency. For each frequency band (delta-theta: 1 – 6 Hz; alpha-beta: 10 – 30 Hz; gamma: 50 – 150 Hz), we then averaged at each channel depth the relative power values across all frequency bins within the band's range, to obtain relative power RP as a function of channel depth (Fig. 1f,i, Fig 5b). For probe recordings in areas where the cortical sheet was inverted due to its anatomical position within a sulcus (i.e., entering from deep to superficial), the channel depths were inverted for all results.

Importantly, the above helped confirm that the spectro-laminar pattern was not an artifact caused by proximity to the cortical surface. First, some of the areas were embedded deep within a sulcus (e.g., MT, MST). Second, depending on the lip within a sulcus, some areas were approached superficial to deep layers, while others were approached by the probe from deep to superficial layers (e.g., MST). The orientation of the spectro-laminar pattern matched the laminar orientation of the area (e.g., probes in MST showed upside-down patterns).

Frequency-based Layer Identification Procedure (FLIP)

The Frequency-based Layer Identification Procedure (FLIP) was designed as a fast, computer-based, fully-automated method to determine the laminar locations of all probe channels in any laminar electrophysiological recording using the LFP signals. After obtaining the average laminar relative power RP as a function of depth for the alpha-beta and gamma bands (see *Power Analysis* Section), we automatically determine whether a probe had an identifiable pattern of opposite alpha-beta / gamma gradients somewhere along the depth range D_i to D_f, where $D_f - D_i = 8$ to 13. For each depth range, we measure the goodness of fit as $G = -(S_{\alpha\beta} * S_{\gamma})$, where $S_{\alpha\beta}$ and S_{γ} are the average slopes of the $RP_{\alpha\beta}$ and RP_{γ} line plots between D_i and D_f. We then repeat the above for all possible depth ranges, and select the maximum goodness of fit G_{max} among them. If G_{max} exceeds the threshold G_t, the probe is classified as having an identifiable alpha-beta / gamma cross-over pattern, and the channels at which the alpha-beta peak, gamma peak, and alpha-beta / gamma cross-over pattern occur are used to map the locations of layers 2/3, 5/6, and 4, respectively. G_t can be optimized depending on the data quality, and is determined by the user by confirming the validity of the classification through visual inspection of the relative power map and the alpha-beta and gamma relative power plots.

Current Source Density (CSD)

Current Source Density (CSD) for each channel along the probe was based on previous work[20] and defined as:

$$CSD(c) = -\sigma \frac{V_{c-2} - 2V_c + V_{c+2}}{(2s)^2}$$

where V is the voltage recorded at channel c, s is the inter-channel spacing and σ is the tissue conductivity. CSD values were normalized by first subtracting the baseline (the average CSD value of 200ms to 0 ms pre-cue/pre-flash), then dividing by the standard error of the mean across trials. This converted the CSD into a unitless measure of z-score units. This can be interpreted as the z-score units of change from baseline, and allows the raw z-score value to express a degree of statistical confidence that a source or a sink was significantly different from baseline.

Image Similarity Analysis

To quantify the degree of similarity between the relative power maps of probe recordings performed within, or between, cortical areas, monkeys, and studies, we employed Image Similarity (IS) analysis, a metric to quantitatively determine the pixel-by-pixel similarity between two images [35]. The images are composed of pixels arranged along a 2-dimensional matrix, where each pixel is defined by a value along a single scale. The resulting IS value ranges between zero (completely dissimilar) and one (identical). The analysis was performed using the Matlab function SSIM. In our study, the pixels of the 2-dimensional images corresponded to the frequency-by-channel matrices of normalized power values, i.e., the relative power maps, with a size of 150 frequency bins by 32 channels. For probes with less than 32 channels and inter-channel spacing higher than

100um, the channels dimension of the relative power maps was resized to 32, interpolating the relative power values spatially to set the inter-channel spacing at 100um.

We compared the relative power maps within each cortical area and between pairs of areas. This was done for all combinations of area pairs within and between monkeys / studies. We randomly subdivided the probes from each area into two equally-sized subsets, and then averaged the relative power maps of all probes in each of the two subset of each area. We computed IS comparing the mean relative power maps between the pair of subsets within each area, and between all four combinations of between-areas pairs of subsets, leading to four between-areas IS estimates. We repeated this probe grouping procedure 5 times, thus obtaining a total of 5 within-area IS values and 20 between-areas IS values. Averaging across these values yielded a grand within-area IS and a grand between-areas IS.

To determine the significance of each of the grand IS values above, we performed the following procedure: we generated 250 randomized versions of each probe by randomly shuffling the channel positions. For each version, we repeated the IS analysis above, obtaining 250 randomized surrogate IS values for each grand IS value. The mean of the 250 randomized surrogate IS values served as an estimate of the degree of similarity that is unrelated to the laminar structure of the relative power maps. Subtracting this value from the grand IS value, we obtained an estimate of the layer-dependent degree of image similarity, which we refer to as laminar IS. The P value for the laminar IS was equal to the fraction of randomized surrogate IS values that were greater than the grand IS value. If $P < 0.05$, the laminar IS value was significantly higher than expected by chance.

To quantify the degree of similarity between the CSD maps, we replicated the entire Image Similarity analysis procedure above on the bidimensional time-by-channel CSD maps as images instead of the relative power maps.

Electrolytic Lesion Approach

To elicit CSD profiles, 70 ms full-screen white flashes were delivered once every 500 ms while tracking eye position. This was repeated between 400-2000 times before selecting target channels for electrolytic lesions. Data were aligned to flash onset, then CSD and relative power profiles were generated. Parameters for electrolytic lesions were similar to previous experiments: monopolar monophasic negative 10–20 uA for 20 sec [38,65]. Current return was through the animal headpost, located at posterior section of the skull. Current was verified on an oscilloscope measuring the voltage across a 10 kohm resistor in series with the stimulation circuit. Care was taken to ensure the stainless-steel shafts of the stimulating Plexon V-probes were not grounded. In monkey St, three lesions were performed (A-M Systems Isolated Pulse Stimulator Model 2100) per probe recording: the first lesion was placed at the most superficial channel that was clearly in brain (sharp increase in spiking or gamma band activity). The second lesion was placed at the prebe channel representing the crossover of alpha-beta and gamma bands. The third lesion was placed at the deepest probe channel. In monkey Sh and Bo only two lesions were made per penetration: one lesion at the “crossover” and one at the deepest channel. This decision was made since the most superficial lesions in monkey St were not visible upon histology – possibly because the current path avoided brain tissue and exited the brain along the surface cerebrospinal fluid to

reach the headpost current return. In monkeys St and Sh, electrolytic lesions were performed in LPFC and LIP. In monkey Bo, lesions were performed in V1 while delivering 70 ms flashes every 250 ms.

Histology

Perfusion surgery

Animal was anesthetized with ketamine (7.5 mg/kg IM) and dexmedetomidine (0.015 mg/kg IM). To provide anatomical landmarks for the electrolytic lesions locations and to later inform the correct slicing plane, angel hair pasta noodles (~1 mm diameter, 13–24 mm into brain) were inserted at the same angle as probe penetrations. In PFC chambers, noodles were placed at medial and posterior coordinates of the chamber. In the Parietal chamber, noodles were placed at medial and anterior chamber coordinates. Lethal sodium pentobarbital solution (40 mg/kg IV or greater) was started immediately after noodle placement. Perfusion surgery details were previously described [66]. Briefly, the animal was perfused transcardially with 30% phosphate buffered saline, followed by 4% paraformaldehyde, and finally 4% paraformaldehyde with 10% sucrose. Whole brain was stored in sucrose phosphate buffered saline until ready for sectioning and slicing. Brain was sectioned along the hemispheric midline and then cut into separate blocks for each chamber. These MRI-guided cuts were estimated to be in plane with noodle and probe penetration angles. Blocks were sliced at 40 μm on a freezing microtome and every other section was stained for Nissl substance.

Imaging

We imaged each Nissl section using a Zeiss Axio Imager.M2 (Jena, Germany) microscope at an imaging magnification factor of 1.25x. This corresponded to a pixel to space conversion factor of eight μm per pixel.

Lesion Identification and Probe Reconstruction

After the creation of the lesions and collection of associated electrophysical data, an individual coordinate system was established in each animal by the placement of two markers (angel hair pasta noodles). Two frames of reference were primarily used to locate lesion locations, the established coordinate system and a set slide order. Other anatomical features, such as the positioning of sulci and gyri, were used to determine positions of each electrolytic lesion in a tissue block. Once located, cortical lesions appeared as roughly circular marks of approximately 100-300um diameter stained a darker purple color compared to the surrounding tissue. In many cases, both or all three lesion marks per probe were identifiable, but in other cases one or no lesion marks were present. In cases where either no electrolytic lesions were identified or only one, we were not able to locate the laminar location of the recording probe. Following identification of each cortical lesion location, we began virtual probe reconstruction, that is, determining probe channel locations with respect to specific cortical layers.

We reconstructed the probe locations by combining the known number of channels, lesion sites, and inter-channel spacing. A virtual probe model was created in accordance with this information, and it was then scaled down using a global factor accounting for tissue shrinkage that occurred during the staining process. The distance between the coordinate markers was measured in the sections and compared to the known distance between them prior to staining. This resulted in a scaling factor of 0.87, meaning that the final imaged tissue had shrunk by 87% compared to the real tissue, comparable to shrinkage in previous reports [67] (Fujimichi et al., Eur J Neurosci, 2010).

A higher number of aligned lesion locations per probe along with punctate, round lesion marks increased confidence of a successful alignment. Using the virtual probe location, electrophysiological data was assigned to each cortical layer. Peaks in the gamma and alpha-beta relative power bands (alpha-beta, 10 – 30 Hz; gamma, 50 – 150 Hz), as well as the cross in alpha-alpha-beta / gamma relative power were identified, and their physical locations were analyzed relative to the cortical layers present. Measurements of the distance from the peaks and crosses in power were taken in micrometer units from the center of cortical layer 4.

References

1. Brodmann, K. (1909). Vergleichende Lokalisationslehre der Grosshirnrinde in ihren Prinzipien dargestellt auf Grund des Zellenbaues (Johann Ambrosius Barth).

2. Binzegger, T., Douglas, R.J., and Martin, K.A.C. (2004). A quantitative map of the circuit of cat primary visual cortex. The Journal of neuroscience *24*, 8441.

3. Douglas, R.J., and Martin, K. (1991). A functional microcircuit for cat visual cortex. The Journal of Physiology *440*, 735.

4. Douglas, R.J., and Martin, K.A.C. (2004). Neuronal Circuits of the Neocortex. Annu. Rev. Neurosci. *27*, 419–451. 10.1146/annurev.neuro.27.070203.144152.

5. Bastos, A.M., Usrey, W.M., Adams, R.A., Mangun, G.R., Fries, P., and Friston, K.J. (2012). Canonical microcircuits for predictive coding. Neuron *76*, 695–711. 10.1016/j.neuron.2012.10.038.

6. Friston, K. (2010). The free-energy principle: a unified brain theory? Nature Reviews Neuroscience *11*, 127–138. 10.1038/nrn2787.

7. Haeusler, S., and Maass, W. (2007). A statistical analysis of information-processing properties of lamina-specific cortical microcircuit models. Cerebral Cortex *17*, 149.

8. Barbas, H., and Rempel-Clower, N (1997). Cortical structure predicts the pattern of corticocortical connections. Cerebral Cortex *7*, 635–646. 10.1093/cercor/7.7.635.

9. Goulas, A., Zilles, K., and Hilgetag, C.C. (2018). Cortical Gradients and Laminar Projections in Mammals. Trends Neurosci. 10.1016/j.tins.2018.06.003.

10. Bastos, A.M., Loonis, R., Kornblith, S., Lundqvist, M., and Miller, E.K. (2018). Laminar recordings in frontal cortex suggest distinct layers for maintenance and control of working memory. PNAS, 201710323. 10.1073/pnas.1710323115.

11. Bollimunta, A., Chen, Y., Schroeder, C.E., and Ding, M. (2008). Neuronal mechanisms of cortical alpha oscillations in awake-behaving macaques. The Journal of Neuroscience *28*, 9976.

12. Buffalo, E.A., Fries, P., Landman, R., Buschman, T.J., and Desimone, R. (2011). Laminar differences in gamma and alpha coherence in the ventral stream. Proceedings of the National Academy of Sciences *108*, 11262.

13. Haegens, S., Barczak, A., Musacchia, G., Lipton, M.L., Mehta, A.D., Lakatos, P., and Schroeder, C.E. (2015). Laminar Profile and Physiology of the α Rhythm in Primary Visual, Auditory, and Somatosensory Regions of Neocortex. J. Neurosci. *35*, 14341–14352. 10.1523/JNEUROSCI.0600-15.2015.

14. van Kerkoerle, T.J., Self, M., Poort, J., van der Togt, C., and Roelfsema, P.R. (2011). High frequencies flow in the feedforward direction through the different layers of monkey primary visual cortex while low frequencies flow in the recurrent direction. In.

15. Lakatos, P., Karmos, G., Mehta, A.D., Ulbert, I., and Schroeder, C.E. (2008). Entrainment of neuronal oscillations as a mechanism of attentional selection. Science *320*, 110–113. 10.1126/science.1154735.

16. Maier, A., Adams, G.K., Aura, C., and Leopold, D.A. (2010). Distinct superficial and deep laminar domains of activity in the visual cortex during rest and stimulation. Frontiers in Systems Neuroscience *4*.

17. Sakata, S., and Harris, K.D. (2009). Laminar Structure of Spontaneous and Sensory-Evoked Population Activity in Auditory Cortex. Neuron *64*, 404–418. 10.1016/j.neuron.2009.09.020.

18. Senzai, Y., Fernandez-Ruiz, A., and Buzsáki, G. (2019). Layer-Specific Physiological Features and Interlaminar Interactions in the Primary Visual Cortex of the Mouse. Neuron *101*, 500-513.e5. 10.1016/j.neuron.2018.12.009.

19. Lefort, S., Tomm, C., Floyd Sarria, J.-C., and Petersen, C.C.H. (2009). The Excitatory Neuronal Network of the C2 Barrel Column in Mouse Primary Somatosensory Cortex. Neuron *61*, 301–316. 10.1016/j.neuron.2008.12.020.

20. Mitzdorf, U., and Singer, W. (1979). Excitatory synaptic ensemble properties in the visual cortex of the macaque monkey: a current source density analysis of electrically evoked potentials. J Comp Neurol *187*, 71–83. 10.1002/cne.901870105.

21. Schroeder, C. (1998). A spatiotemporal profile of visual system activation revealed by current source density analysis in the awake macaque. Cerebral Cortex *8*, 575–592. 10.1093/cercor/8.7.575.

22. Schroeder, C.E., Tenke, C.E., Givre, S.J., Arezzo, J.C., and Vaughan, H.G. (1991). Striate cortical contribution to the surface-recorded pattern-reversal VEP in the alert monkey. Vision Res. *31*, 1143–1157.

23. Constantinople, C.M., and Bruno, R.M. (2013). Deep cortical layers are activated directly by thalamus. Science *340*, 1591–1594. 10.1126/science.1236425.

24. Godlove, D.C., Maier, A., Woodman, G.F., and Schall, J.D. (2014). Microcircuitry of agranular frontal cortex: testing the generality of the canonical cortical microcircuit. J. Neurosci. *34*, 5355–5369. 10.1523/JNEUROSCI.5127-13.2014.

25. van Kerkoerle, T., Self, M.W., Dagnino, B., Gariel-Mathis, M.-A., Poort, J., van der Togt, C., and Roelfsema, P.R. (2014). Alpha and gamma oscillations characterize feedback and feedforward processing in monkey visual cortex. Proc. Natl. Acad. Sci. U.S.A. *111*, 14332–14341. 10.1073/pnas.1402773111.

26. Roopun, A.K., Kramer, M.A., Carracedo, L.M., Kaiser, M., Davies, C.H., Traub, R.D., Kopell, N.J., and Whittington, M.A. (2008). Period concatenation underlies interactions between gamma and beta rhythms in neocortex. Front Cell Neurosci *2*, 1. 10.3389/neuro.03.001.2008.

27. Smith, M.A., Jia, X., Zandvakili, A., and Kohn, A. (2013). Laminar dependence of neuronal correlations in visual cortex. J. Neurophysiol. *109*, 940–947. 10.1152/jn.00846.2012.

28. Spaak, E., Bonnefond, M., Maier, A., Leopold, D.A., and Jensen, O. (2012). Layer-specific entrainment of γ-band neural activity by the α rhythm in monkey visual cortex. Curr. Biol. *22*, 2313–2318. 10.1016/j.cub.2012.10.020.

29. Barzegaran, E., and Plomp, G. (2022). Four concurrent feedforward and feedback networks with different roles in the visual cortical hierarchy. PLOS Biology *20*, e3001534. 10.1371/journal.pbio.3001534.

30. Bastos, A.M., Vezoli, J., Bosman, C.A., Schoffelen, J.-M., Oostenveld, R., Dowdall, J.R., De Weerd, P., Kennedy, H., and Fries, P. (2015). Visual areas exert feedforward and feedback influences through distinct frequency channels. Neuron *85*, 390–401. 10.1016/j.neuron.2014.12.018.

31. Mejias, J.F., Murray, J.D., Kennedy, H., and Wang, X.-J. (2016). Feedforward and feedback frequency-dependent interactions in a large-scale laminar network of the primate cortex. Science Advances *2*, e1601335–e1601335. 10.1126/sciadv.1601335.

32. Michalareas, G., Vezoli, J., van Pelt, S., Schoffelen, J.-M., Kennedy, H., and Fries, P. (2016). Alpha-Beta and Gamma Rhythms Subserve Feedback and Feedforward Influences among Human Visual Cortical Areas. Neuron *89*, 384–397. 10.1016/j.neuron.2015.12.018.

33. Johnston, K., Ma, L., Schaeffer, L., and Everling, S. (2019). Alpha Oscillations Modulate Preparatory Activity in Marmoset Area 8Ad. J. Neurosci. *39*, 1855–1866. 10.1523/JNEUROSCI.2703-18.2019.

34. Halgren, M., Ulbert, I., Bastuji, H., Fabó, D., Erőss, L., Rey, M., Devinsky, O., Doyle, W.K., Mak-McCully, R., Halgren, E., et al. (2019). The generation and propagation of the human alpha rhythm. PNAS *116*, 23772–23782. 10.1073/pnas.1913092116.

35. Wang, Z., Bovik, A.C., Sheikh, H.R., and Simoncelli, E.P. (2004). Image quality assessment: from error visibility to structural similarity. IEEE Transactions on Image Processing *13*, 600–612. 10.1109/TIP.2003.819861.

36. van Kerkoerle, T., Self, M.W., and Roelfsema, P.R. (2017). Layer-specificity in the effects of attention and working memory on activity in primary visual cortex. Nat Commun *8*, 13804. 10.1038/ncomms13804.

37. Maier, A., Adams, G.K., Aura, C., and Leopold, D.A. (2010). Distinct superficial and deep laminar domains of activity in the visual cortex during rest and stimulation. Frontiers in Systems Neuroscience *4*.

38. Takeuchi, D., Hirabayashi, T., Tamura, K., and Miyashita, Y. (2011). Reversal of interlaminar signal between sensory and memory processing in monkey temporal cortex. Science *331*, 1443–1447. 10.1126/science.1199967.

39. Westerberg, J.A., Cox, M.A., Dougherty, K., and Maier, A. (2019). V1 microcircuit dynamics: altered signal propagation suggests intracortical origins for adaptation in response to visual repetition. J. Neurophysiol. *121*, 1938–1952. 10.1152/jn.00113.2019.

40. Balaram, P., and Kaas, J.H. (2014). Towards a unified scheme of cortical lamination for primary visual cortex across primates: insights from NeuN and VGLUT2 immunoreactivity. Frontiers in Neuroanatomy *8*.

41. Wagstyl, K., Larocque, S., Cucurull, G., Lepage, C., Cohen, J.P., Bludau, S., Palomero-Gallagher, N., Lewis, L.B., Funck, T., Spitzer, H., et al. (2020). BigBrain 3D atlas of cortical layers: Cortical and laminar thickness gradients diverge in sensory and motor cortices. PLOS Biology *18*, e3000678. 10.1371/journal.pbio.3000678.

42. Lundqvist, M., Bastos, A.M., and Miller, E.K. (2020). Preservation and Changes in Oscillatory Dynamics across the Cortical Hierarchy. Journal of Cognitive Neuroscience *32*, 2024–2035. 10.1162/jocn_a_01600.

43. Bonaiuto, J.J., Meyer, S.S., Little, S., Rossiter, H., Callaghan, M.F., Dick, F., Barnes, G.R., and Bestmann, S. (2018). Lamina-specific cortical dynamics in human visual and sensorimotor cortices. eLife *7*, e33977. 10.7554/eLife.33977.

44. Scheeringa, R., Koopmans, P.J., Mourik, T. van, Jensen, O., and Norris, D.G. (2016). The relationship between oscillatory EEG activity and the laminar-specific BOLD signal. Proceedings of the National Academy of Sciences of the United States of America *113*, 6761. 10.1073/pnas.1522577113.

45. Bollimunta, A., Mo, J., Schroeder, C.E., and Ding, M. (2011). Neuronal Mechanisms and Attentional Modulation of Corticothalamic Alpha Oscillations. The Journal of Neuroscience *31*, 4935.

46. Cunningham, M.O., Whittington, M.A., Bibbig, A., Roopun, A., LeBeau, F.E.N., Vogt, A., Monyer, H., Buhl, E.H., and Traub, R.D. (2004). A role for fast rhythmic bursting neurons in cortical gamma oscillations in vitro. Proceedings of the National Academy of Sciences *101*, 7152–7157. 10.1073/pnas.0402060101.

47. Yamawaki, N., Stanford, I.M., Hall, S.D., and Woodhall, G.L. (2008). Pharmacologically induced and stimulus evoked rhythmic neuronal oscillatory activity in the primary motor cortex in vitro. Neuroscience *151*, 386–395. 10.1016/j.neuroscience.2007.10.021.

48. Westerberg, J.A., Sigworth, E.A., Schall, J.D., and Maier, A. (2021). Pop-out search instigates beta-gated feature selectivity enhancement across V4 layers. Proceedings of the National Academy of Sciences *118*, e2103702118. 10.1073/pnas.2103702118.

49. Felleman, D.J., and Van Essen, D.C. (1991). Distributed hierarchical processing in the primate cerebral cortex. Cerebral cortex *1*, 1–47.

50. Markov, N.T., Vezoli, J., Chameau, P., Falchier, A., Quilodran, R., Huissoud, C., Lamy, C., Misery, P., Giroud, P., Ullman, S., et al. (2013). The anatomy of hierarchy: Feedforward and feedback pathways in macaque visual cortex. J. Comp. Neurol. 10.1002/cne.23458.

51. Miller, E.K., Lundqvist, M., and Bastos, A.M. (2018). Working Memory 2.0. Neuron *100*, 463–475. 10.1016/j.neuron.2018.09.023.

52. Dalal, S.S., Edwards, E., Kirsch, H.E., Barbaro, N.M., Knight, R.T., and Nagarajan, S.S. (2008). Localization of neurosurgically implanted electrodes via photograph–MRI–radiograph coregistration. Journal of Neuroscience Methods *174*, 106–115. 10.1016/j.jneumeth.2008.06.028.

53. Oxenford, S., Roediger, J., Neudorfer, C., Milosevic, L., Güttler, C., Spindler, P., Vajkoczy, P., Neumann, W.-J., Kühn, A., and Horn, A. (2022). Lead-OR: A multimodal platform for deep brain stimulation surgery. eLife *11*, e72929. 10.7554/eLife.72929.

54. Lebedev, M.A., and Nicolelis, M.A.L. (2017). Brain-Machine Interfaces: From Basic Science to Neuroprostheses and Neurorehabilitation. Physiological Reviews *97*, 767–837. 10.1152/physrev.00027.2016.

55. Little, S., and Brown, P. (2014). The functional role of beta oscillations in Parkinson's disease. Parkinsonism & Related Disorders *20*, S44–S48. 10.1016/S1353-8020(13)70013-0.

56. Cho, K.K.A., Hoch, R., Lee, A.T., Patel, T., Rubenstein, J.L.R., and Sohal, V.S. (2015). Gamma Rhythms Link Prefrontal Interneuron Dysfunction with Cognitive Inflexibility in Dlx5/6+/− Mice. Neuron *85*, 1332–1343. 10.1016/j.neuron.2015.02.019.

57. Cho, R.Y., Konecky, R.O., and Carter, C.S. (2006). Impairments in frontal cortical gamma synchrony and cognitive control in schizophrenia. Proc. Natl. Acad. Sci. U.S.A. *103*, 19878–19883. 10.1073/pnas.0609440103.

58. Adaikkan, C., Middleton, S.J., Marco, A., Pao, P.-C., Mathys, H., Kim, D.N.-W., Gao, F., Young, J.Z., Suk, H.-J., Boyden, E.S., et al. (2019). Gamma Entrainment Binds Higher-Order Brain Regions and Offers Neuroprotection. Neuron *102*, 929-943.e8. 10.1016/j.neuron.2019.04.011.

59. Jun, J.J., Steinmetz, N.A., Siegle, J.H., Denman, D.J., Bauza, M., Barbarits, B., Lee, A.K., Anastassiou, C.A., Andrei, A., Aydın, Ç., et al. (2017). Fully integrated silicon probes for high-density recording of neural activity. Nature *551*, 232–236. 10.1038/nature24636.

60. Ruiz, O., Lustig, B.R., Nassi, J.J., Cetin, A., Reynolds, J.H., Albright, T.D., Callaway, E.M., Stoner, G.R., and Roe, A.W. (2013). Optogenetics through windows on the brain in the nonhuman primate. J. Neurophysiol. *110*, 1455–1467. 10.1152/jn.00153.2013.

61. Mulliken, G.H., Bichot, N.P., Ghadooshahy, A., Sharma, J., Kornblith, S., Philcock, M., and Desimone, R. (2015). Custom-fit radiolucent cranial implants for neurophysiological recording and stimulation. J. Neurosci. Methods *241*, 146–154. 10.1016/j.jneumeth.2014.12.011.

62. Bastos, A.M., Lundqvist, M., Waite, A.S., Kopell, N., and Miller, E.K. (2020). Layer and rhythm specificity for predictive routing. Proc Natl Acad Sci U S A *117*, 31459–31469. 10.1073/pnas.2014868117.

63. Oostenveld, R., Fries, P., Maris, E., and Schoffelen, J.-M. (2011). FieldTrip: Open source software for advanced analysis of MEG, EEG, and invasive electrophysiological data. Comput Intell Neurosci *2011*, 156869. 10.1155/2011/156869.

64. Mitra, P.P., and Pesaran, B. (1999). Analysis of dynamic brain imaging data. Biophys. J. *76*, 691–708. 10.1016/S0006-3495(99)77236-X.

65. Graziano, M.S.A., Taylor, C.S.R., and Moore, T. (2002). Complex Movements Evoked by Microstimulation of Precentral Cortex. Neuron *34*, 841–851. 10.1016/S0896-6273(02)00698-0.

66. Wu, C.W.-H., Bichot, N.P., and Kaas, J.H. (2000). Converging evidence from microstimulation, architecture, and connections for multiple motor areas in the frontal and cingulate cortex of prosimian primates. Journal of Comparative Neurology *423*, 140–177. 10.1002/1096-9861(20000717)423:1<140::AID-CNE12>3.0.CO;2-3.

67. Yoshida, M., Naya, Y., and Miyashita, Y. (2003). Anatomical organization of forward fiber projections from area TE to perirhinal neurons representing visual long-term memory in monkeys. Proceedings of the National Academy of Sciences *100*, 4257–4262. 10.1073/pnas.0736457100.

Acknowledgements

We thank Carolyn Wu, Jefferson Roy and Huixin Qi for assistance with perfusions and brain fixation and extraction; Haoran Xu for assistance with surgical procedures for Study 2; Jon Kaas and Laura Trice for assistance with histological processing; Micala Maddox for assistance with monkey Bo; Meredith Mahnke for help with behavioral training and implant maintenance for Study 1; animal care and the veterinarian staff at MIT and Vanderbilt for their assistance with and care for the animals. This work was supported by NIH EY017921 (RD), NIMH R37MH087027 (EKM), NIMH R00MH116100 (AMB), R01EY027402 (AMaier), T32EY007135 (BM), and F31EY031293 (JW).

Author Contributions

Electrophysiology data collection, study 1: AMB
Electrophysiology data collection, study 2: DMH
Electrophysiology data analysis: NL, AMajor, DMH, AMB
Electrophysiology data collection for additional areas, and electrolytic lesion experiments: AMajor, BC, BM, JW, AMaier, AMB
Histology tissue processing and imaging: ML, YSX, JW, PDM
Histology data analysis: ML, AMB
Advice and assistance on histology processing: JK
Funding acquisition, Study 1: EKM
Funding acquisition, Study 2: RD
Funding acquisition, V1 data: AMaier
Funding acquisition, Histology: AMB
Study design: DMH, EKM, RD, AMB
Writing, first draft: DMH, AMB
Writing, revised draft: All authors

Supplementary Figures

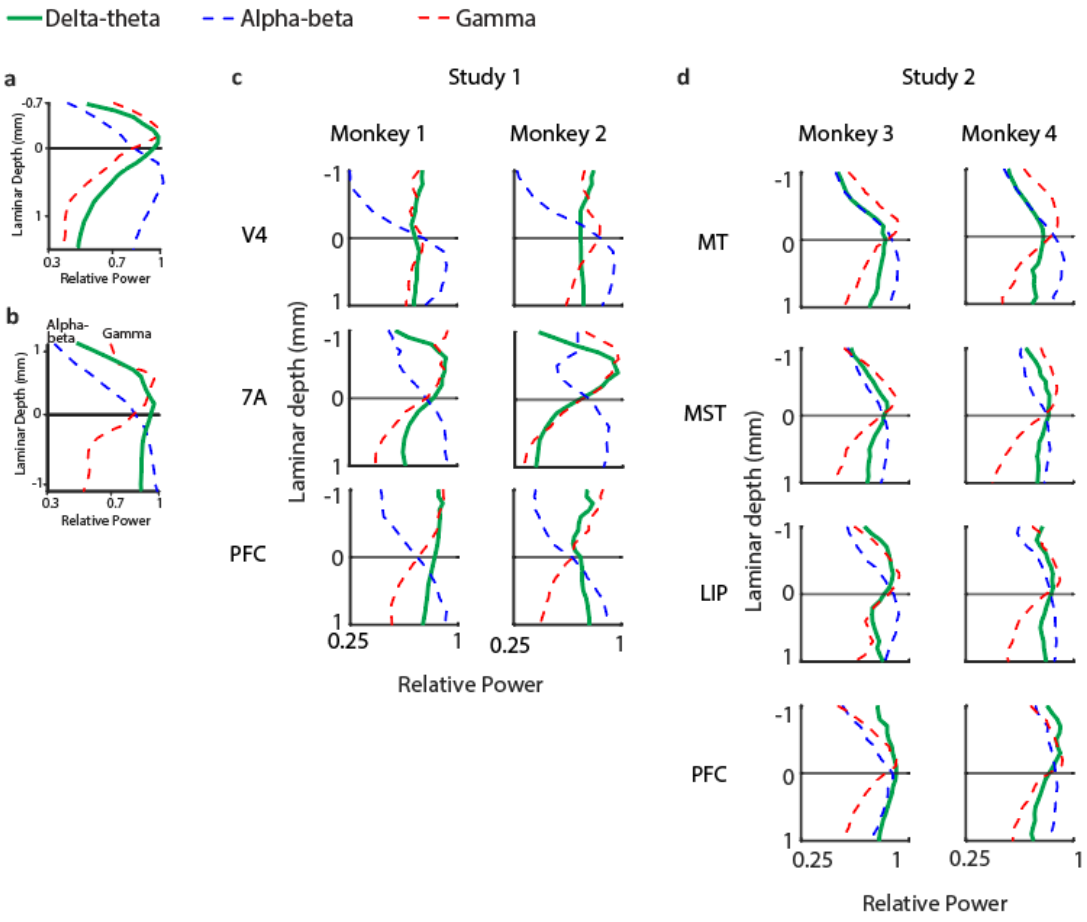

Supplementary Figure 1. Relative power in the delta-theta (green line) frequency band as a function of laminar depth for two example probes (a,b), and averaged across probes from each area in Study 1 (c) and Study 2 (d). Relative power in the alpha-beta (dotted blue line) and gamma (dashed red line) bands are shown for comparison.

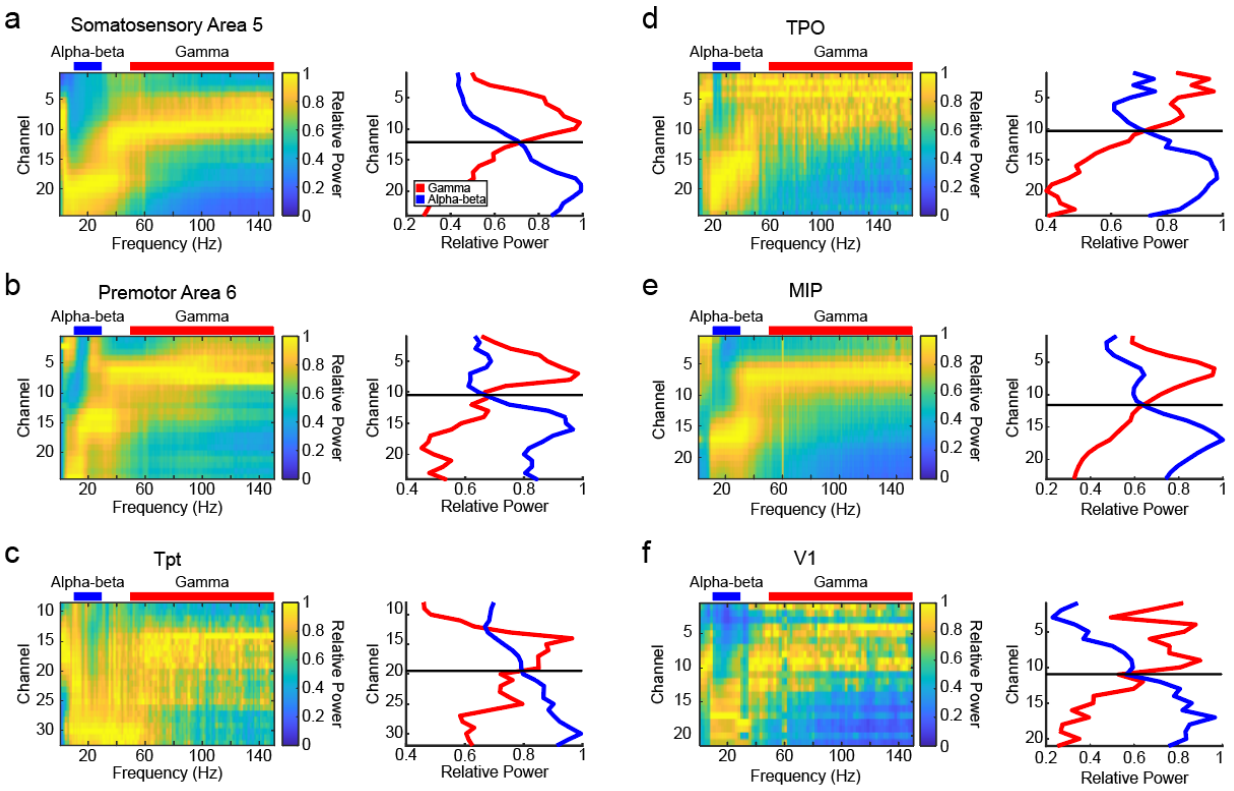

Supplementary Figure 2. Spectrolaminar pattern is preserved in additional recorded areas: (a) somatosensory area 5, (b) premotor area 6, (c) temporo-parietal area (Tpt), (d) temporal-parietal-occipital area (TPO), (e) medial intraparietal area (MIP), (f) primary visual cortex (V1). For each area, left subplot shows relative power map, and right subplot shows average relative power in the alpha-beta (blue) and gamma (red) bands as a function of laminar depth for an example probe.

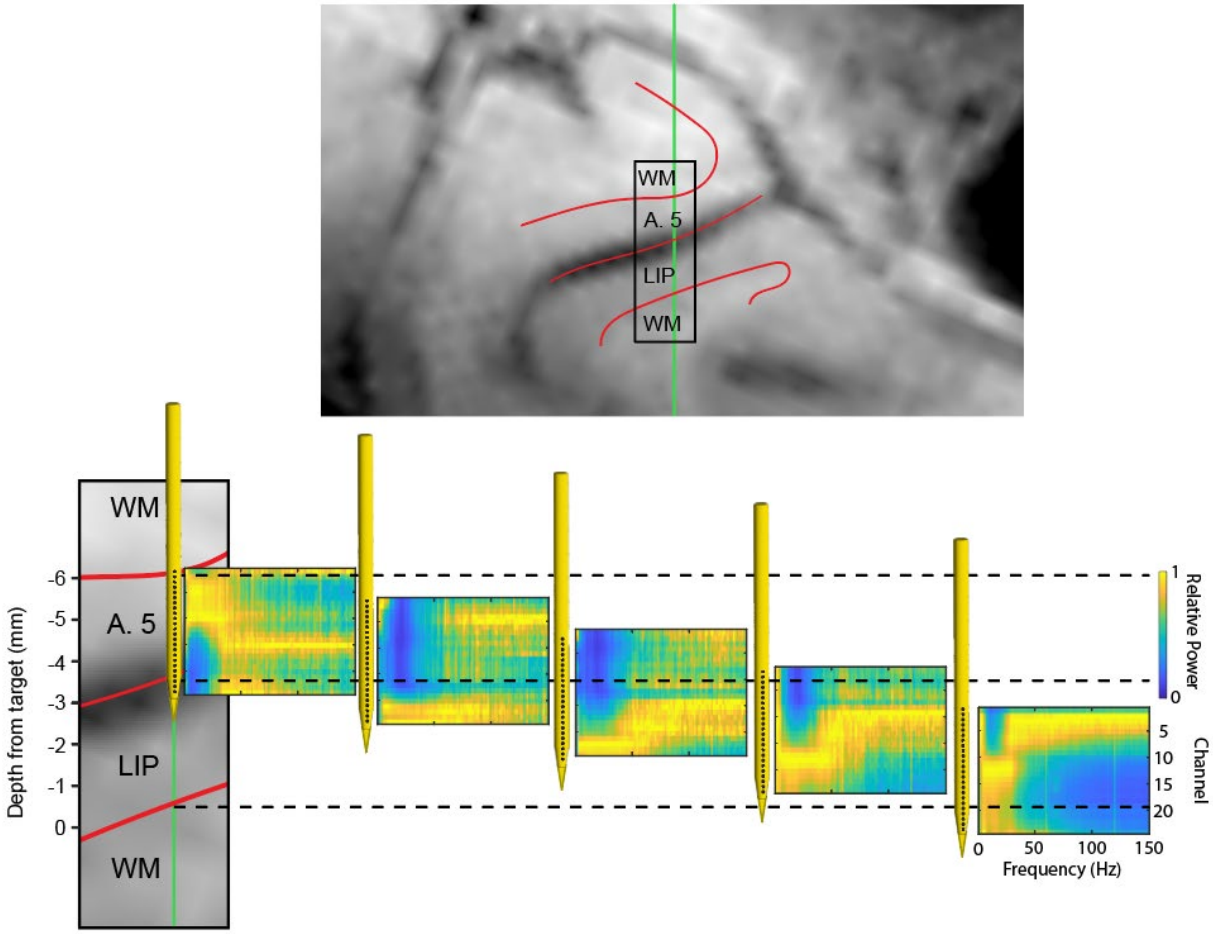

Supplementary Figure 3. Transformation of relative power map during probe implantation in the cortex. Top: structural MRI section showing probe trajectory (green) across cortical layers in Areas 5 and LIP. Bottom: Magnification of black rectangular region above, and corresponding relative power maps recorded at various probe depths. An inverted "swoosh" spectrolaminar pattern appears when the probe crosses the layers of Area 5 in a deep-to-superficial direction. Subsequently, an upright pattern appears gradually as the probe crosses the layers of LIP in a superficial-to-deep direction. The last map was acquired with the probe in the same position as the previous, but after waiting 1 hour; the cortex appears to relax after having dimpled during penetration, creating the illusion that the probe moved deeper. Examining the spectrolaminar patterns in close-to-real time during probe implantation provides the experimenter with a more precise method to track the probe position with respect to cortical sheets/layers than using previously-acquired MRI images for guidance. GM, gray matter; WM, white matter.

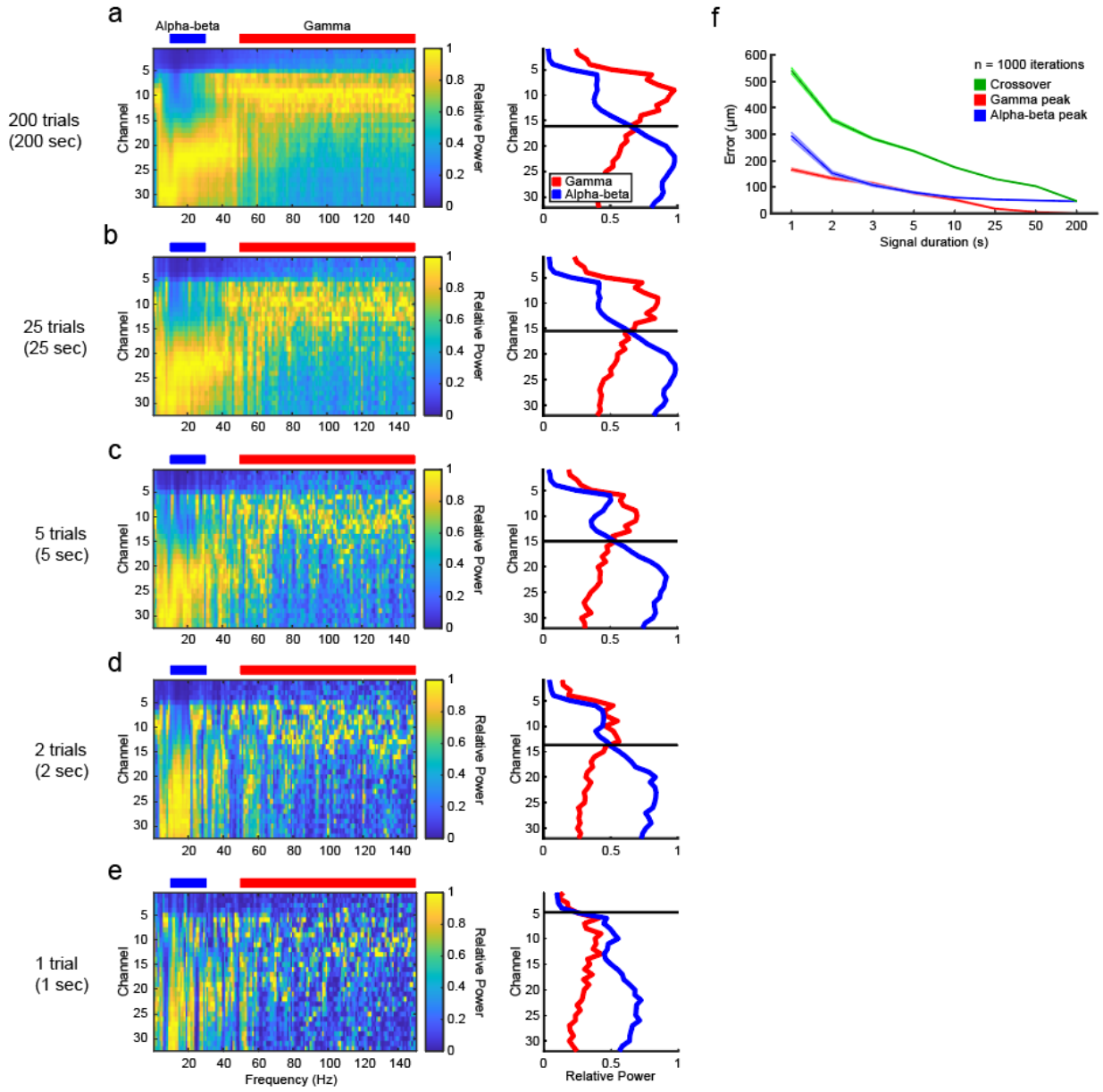

Supplementary Figure 4. Quality of spectrolaminar pattern as a function of signal duration. (a-e), Relative power map (left subplot) and average relative power in the alpha-beta (blue) and gamma (red) bands (right subplot) from an example probe, obtained from signals of varying durations: 200 s, 25 s, 5 s, 3 s, 2 s, and 1 s. The spectrolaminar pattern quality decreases with decreasing signal duration, but it is still detectable in signals of a few seconds. (f) Mean (+/- SEM over 1000 iteration of data selection) error in estimating the location of gamma peak, alpha-beta peak, and crossover as a function of signal duration. Errors are measured with respect to the locations obtained from analyzing all trials recorded (> 200).

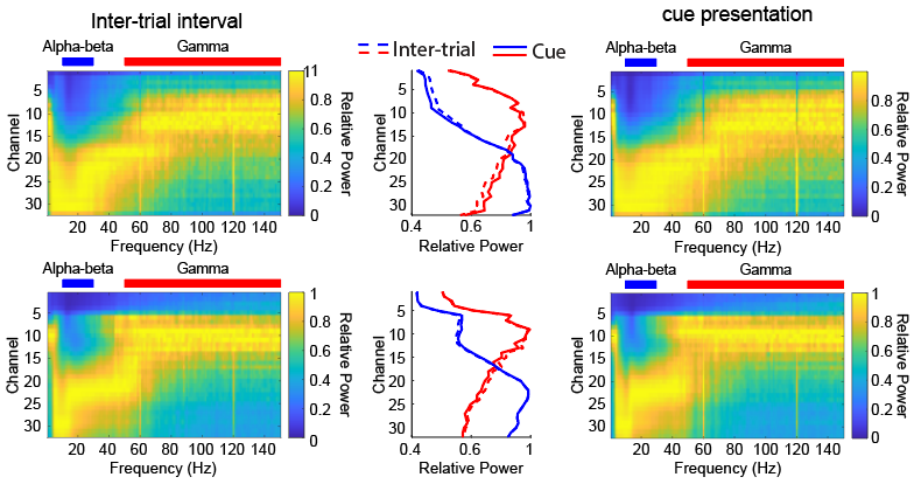

Supplementary Figure 5. Spectrolaminar pattern during visual stimulation vs inter-trial interval. Relative power map during inter-trial interval (left column, 1 s before fixation onset until fixation onset) and during cue presentation period (right columns, first 500 ms of cue presentation), and average relative power in the alpha-beta (blue) and gamma (red) bands (middle column) for two example recordings (top and bottom).

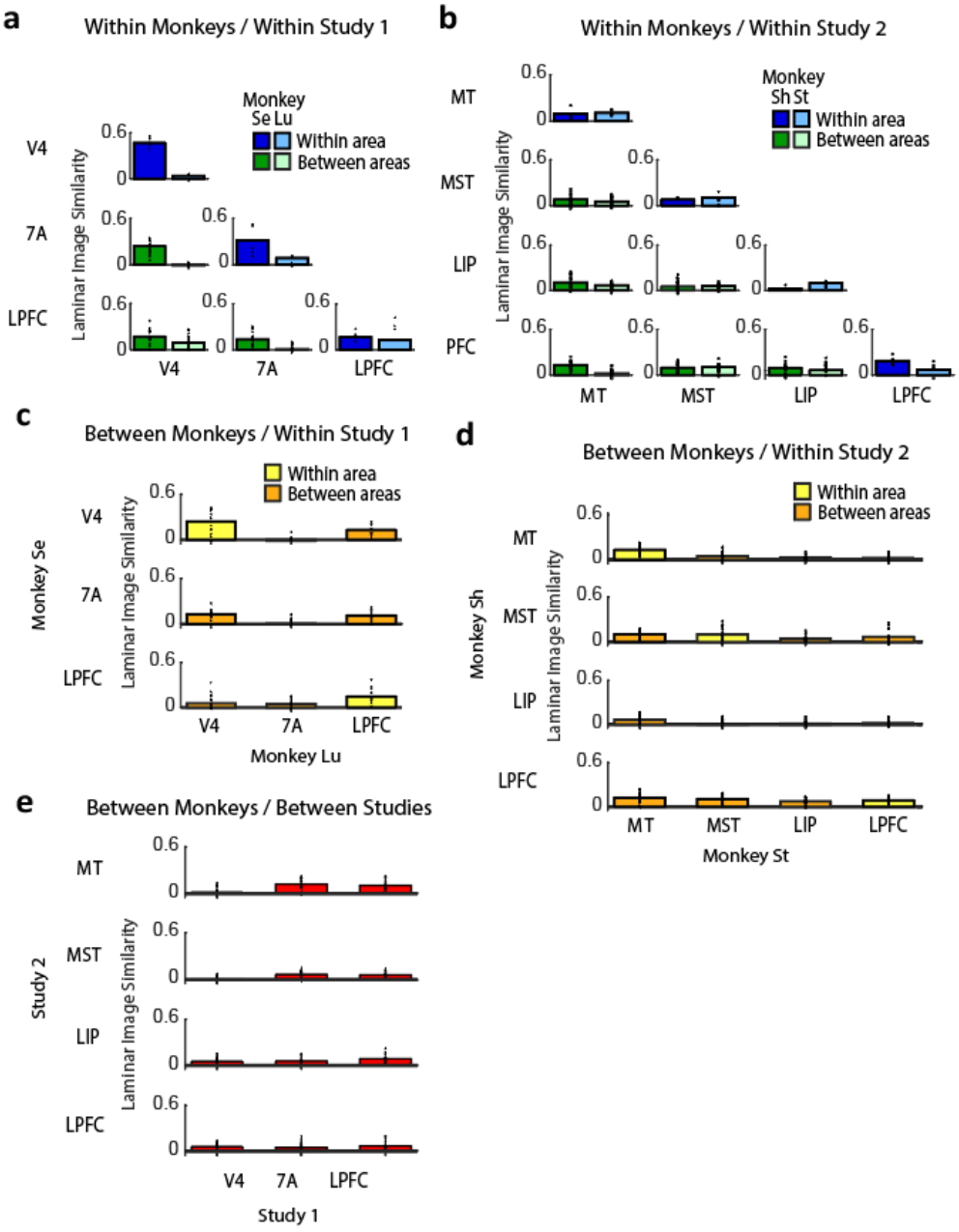

Supplementary Figure 6. Similarity between CSD maps within and between cortical areas, monkeys and studies. (a,b) Mean laminar image similarity of CSD maps across probe recordings within (blue) and between (green) areas within each monkey within Study 1 (a) and Study 2 (b). (c,d) Mean laminar image similarity within (yellow) and between (orange) areas between monkeys within Study 1 (c) and Study 2 (d). (e) Mean laminar image similarity between areas, between monkeys and between studies. (A-E) The height of each bar corresponds to the Mean laminar image similarity across all randomized probe splits (individual dots; see Methods).

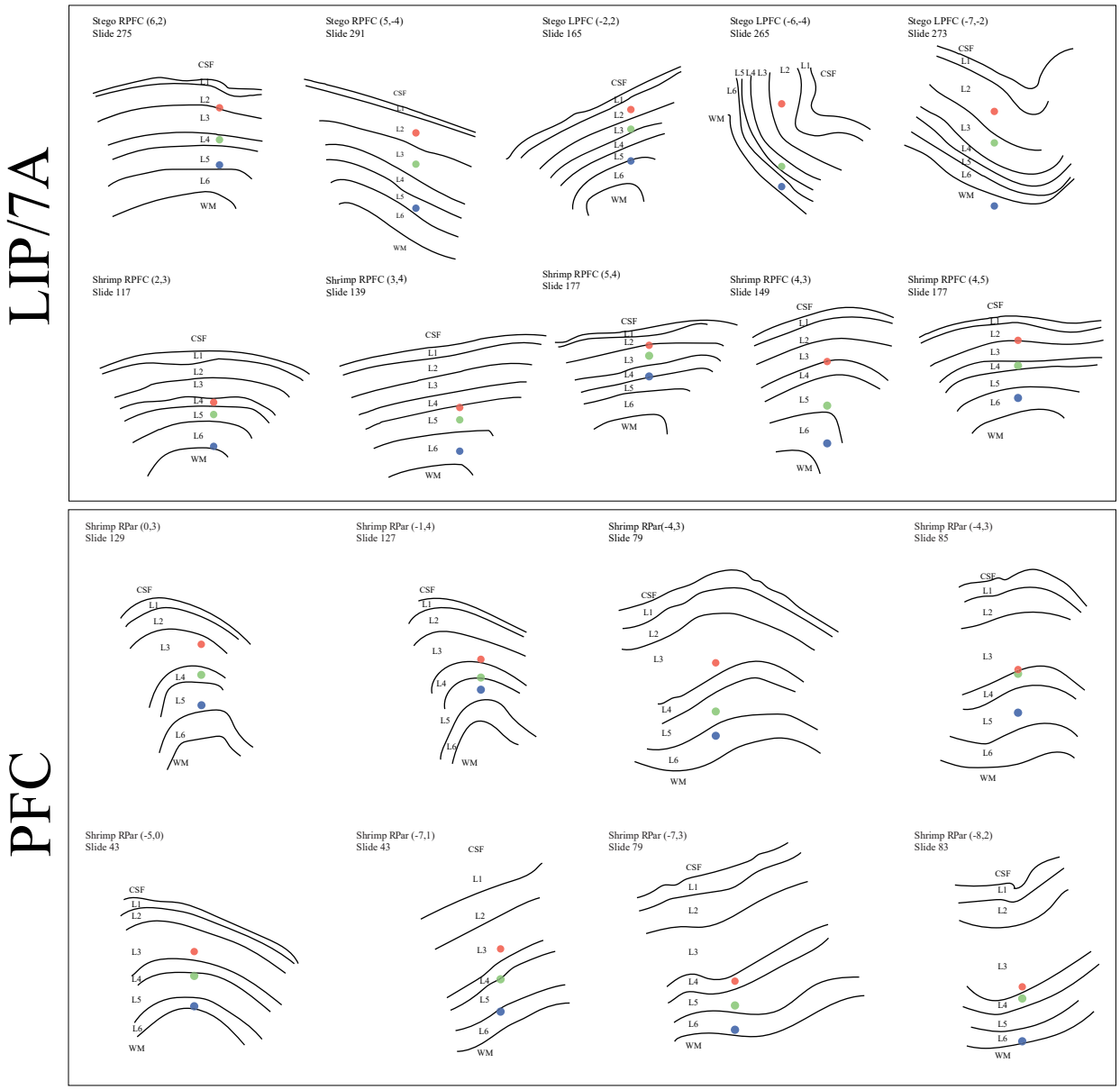

Supplementary Figure 7. Individual anatomical probe reconstructions for Parietal and Prefrontal Cortex. *Upper panel*, traces of individual brain slices are shown for area 7A/LIP with anatomically-defined layers labelled from CSF (cerebrospinal fluid), layer 1–6 (L1–L6), and WM (white matter). Each example includes monkey name, brain region, probe grid location, and histological slice number. Red, green, and blue dots correspond to gamma peak, relative power crossover, and alpha-beta peak, respectively. *Lower panel*, traces of individual brain slices are shown for dorsolateral and ventrolateral prefrontal cortex. LIP, lateral intraparietal area; PFC, prefrontal cortex.

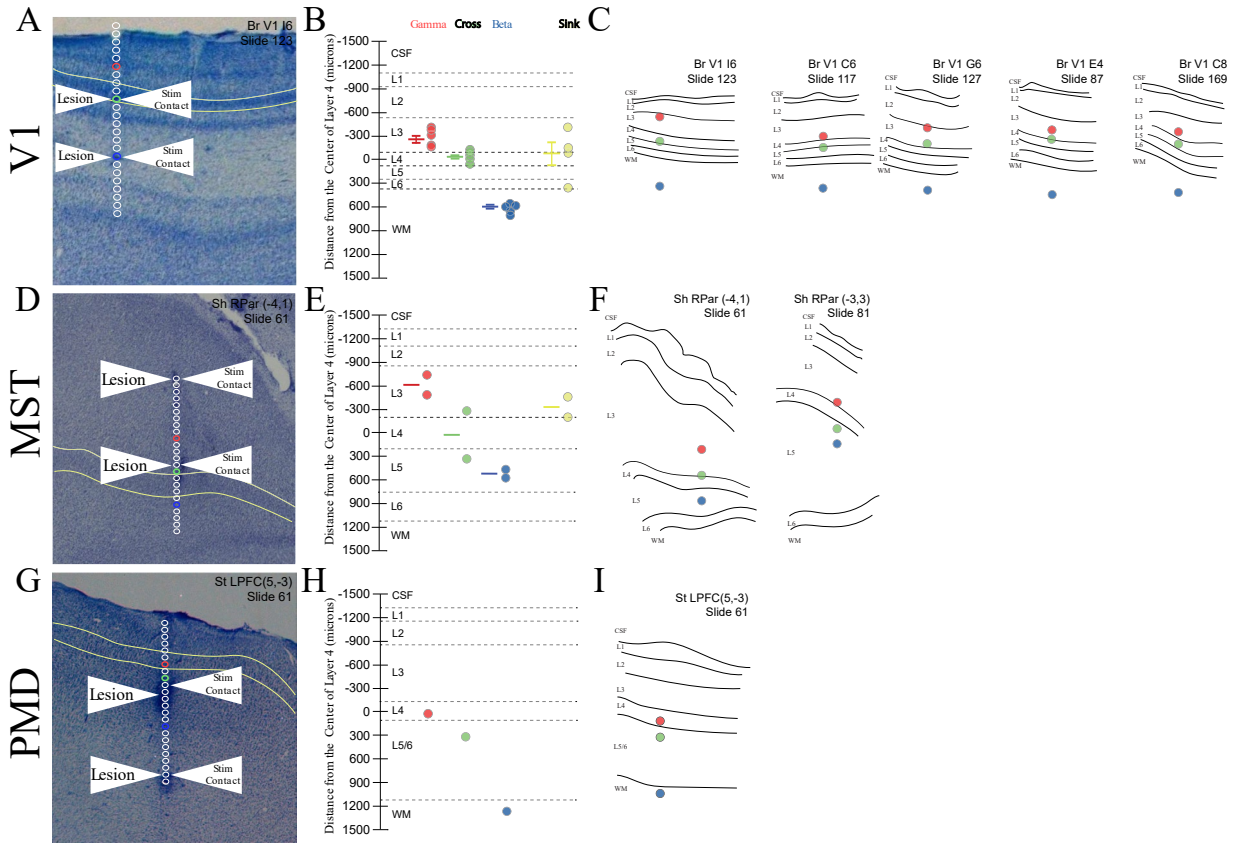

Supplementary Figure 8. Histological results and examples from V1, MST, and PMD. *A*, example histological slice from primary visual area (V1). Identification of electrolytic lesions allows reconstruction of all channels of the laminar probe, shown as open circles. Red circle represents probe contact with gamma power peak, green circle represents crossover, and blue circle represents alpha-beta peak. Green curves lines demarcate layer 4. *B*, Population results from V1 histological reconstruction (n = 5). Gamma peak (red), crossover (green), alpha-beta peak (blue), and current source density sink (yellow) are shown as distances from center of anatomically-determined layer 4 (mean +/- SEM). Negative values indicate more superficial locations, towards layer 1 and CSF (cerebrospinal fluid). *C*, Individual anatomical probe reconstructions for primary visual cortex. Same format as in Supplementary Figure 7. *D–F*, example histological slices and reconstructed electrophysiological results from middle superior temporal area (MST). *G–I*, example histological slice and reconstructed electrophysiological results from dorsal premotor cortex (PMD).